On the Predictability of Sea Surface Height around Palau

MAGDALENA ANDRES,[a] RUTH C. MUSGRAVE,[a,b] DANIEL L. RUDNICK,[c] KRISTIN L. ZEIDEN,[c] THOMAS PEACOCK,[d] AND JAE-HUN PARK[e]

[a] *Woods Hole Oceanographic Institution, Woods Hole, Massachusetts*
[b] *Dalhousie University, Halifax, Nova Scotia, Canada*
[c] *Scripps Institution of Oceanography, La Jolla, California*
[d] *Massachusetts Institute of Technology, Cambridge, Massachusetts*
[e] *Inha University, Incheon, South Korea*

(Manuscript received 23 December 2019, in final form 17 June 2020)

ABSTRACT

As part of the Flow Encountering Abrupt Topography (FLEAT) program, an array of pressure-sensor equipped inverted echo sounders (PIESs) was deployed north of Palau where the westward-flowing North Equatorial Current encounters the southern end of the Kyushu–Palau Ridge in the tropical North Pacific. Capitalizing on concurrent observations from satellite altimetry, FLEAT Spray gliders, and shipboard hydrography, the PIESs' 10-month duration hourly bottom pressure p and round-trip acoustic travel time τ records are used to examine the magnitude and predictability of sea level and pycnocline depth changes and to track signal propagations through the array. Sea level and pycnocline depth are found to vary in response to a range of ocean processes, with their magnitude and predictability strongly process dependent. Signals characterized here comprise the barotropic tides, semidiurnal and diurnal internal tides, southeastward-propagating superinertial waves, westward-propagating mesoscale eddies, and a strong signature of sea level increase and pycnocline deepening associated with the region's relaxation from El Niño to La Niña conditions. The presence of a broad band of superinertial waves just above the inertial frequency was unexpected and the FLEAT observations and output from a numerical model suggest that these waves detected near Palau are forced by remote winds east of the Philippines. The PIES-based estimates of pycnocline displacement are found to have large uncertainties relative to overall variability in pycnocline depth, as localized deep current variations arising from interactions of the large-scale currents with the abrupt topography around Palau have significant travel time variability.

1. Introduction

Oceanic processes that have an expression in sea surface height (SSH) occur over a range of time scales. Since the early 1990s satellite altimetry has been used to examine SSH variability related to processes at intraseasonal periods such as mesoscale eddy motions (Chelton et al. 2011) or baroclinic Rossby wave propagations (Qiu and Chen 2005) and at longer periods, including studies of regional and global sea level rise (Church and White 2011). Some higher-frequency signals have also been investigated with altimetry by capitalizing on their fixed periods, notably the SSH signal associated with the stationary part of the baroclinic tides (Ray and Mitchum 1997). However, high-frequency SSH variability that is not associated with fixed periods or phases, like the surface expression of the internal wave field, is not well resolved by the space–time sampling of the present constellation of altimeters. In situ observations that can resolve these time scales are needed to help elucidate processes and ground truth numerical models.

Here we use satellite altimetry together with in situ data to examine SSH variability at time scales ranging from tidal to interannual near Palau, an island group at the southern end of the Kyushu–Palau Ridge in the western North Pacific (Fig. 1), which sits near the boundary between the westward-flowing North Equatorial Current (NEC) and the eastward-flowing

Denotes content that is immediately available upon publication as open access.

Corresponding author: Magdalena Andres, mandres@whoi.edu

DOI: 10.1175/JPO-D-19-0310.1

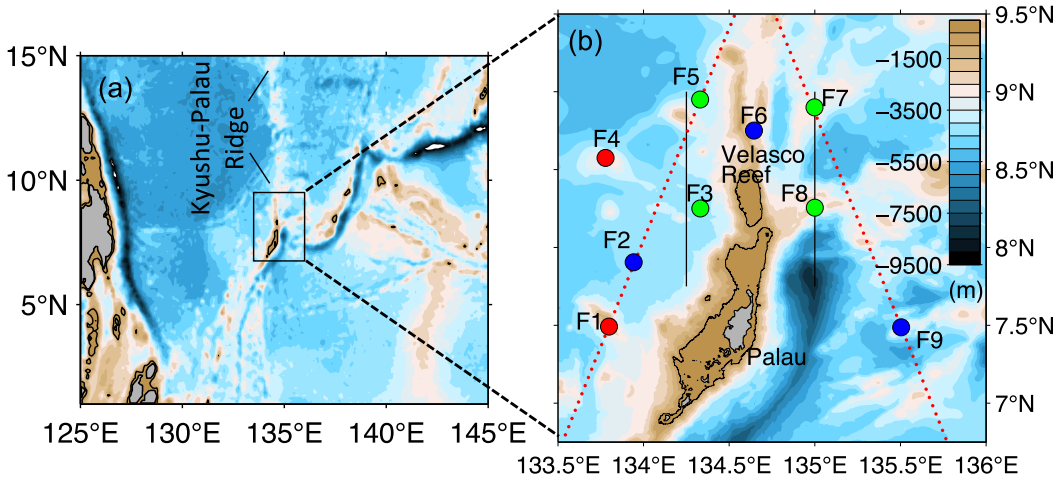

FIG. 1. (a) Map of the western tropical North Pacific Ocean with (b) a closeup showing the FLEAT instrument locations F1–F9 with the bathymetry shaded (m) and the 500-m isobath (black contour), satellite altimeter reference tracks (red dotted lines), standard PIES sites (blue circles), CPIES sites (green circles), RPIES sites (red circles), and Spray glider tracks (black lines).

North Equatorial Countercurrent (NECC). We use the observations to investigate the following questions: What are the key drivers of SSH variability near Palau? How much do these processes each contribute to the overall SSH field, and what part of the SSH field is predictable? Further, how does the steep topography and complicated current system around Palau affect the SSH signal propagation there and how is variability in SSH related to variability in the pycnocline?

To help address these questions, an array of in situ instruments was deployed on the seabed for 10 months around the northern half of Palau. This deployment was part of an integrated observational and modeling campaign called Flow Encountering Abrupt Topography (FLEAT), funded by the U.S. Office of Naval Research. The overall goals of FLEAT include 1) investigating processes that drive the downscale cascade of energy, 2) examining interactions between the upper and deep ocean, and 3) exploring the role of topography in shaping the flow (Johnston et al. 2019).

Using the observations, we show that a range of processes affect the sea surface in this region (Fig. 2). The processes discussed here comprise (from largest to smallest SSH signal) the barotropic tides (with a small SSH contribution also from internal tides), interannual signals related to El Niño–Southern Oscillation (ENSO), mesoscale eddies, and a superinertial signal (i.e., with frequencies higher than the local inertial frequency f). Each of these processes (except the barotropic tide) also has an expression in the pycnocline. We demonstrate that the predictability of the SSH and pycnocline signals are highly process dependent.

Measurements from our bottom-moored instruments and other datasets used in this study are introduced in section 2. Methods used to process and interpret these data are explained in section 2 and an appendix. We present our results in section 3. These include descriptions of tidal variability separated into surface (barotropic) and internal (baroclinic) components as well as descriptions of nontidal variability in the sea surface and pycnocline depth inferred from the in situ measurements around Palau. This section discusses variability observed with the FLEAT array in a superinertial band (1.1–3 days) and in the mesoscale band (20–100 days) and also considers the FLEAT experiment period in the context of longer-term interannual variability in the region associated with El Niño Southern Oscillation (ENSO) cycles. Our findings about the amplitude and predictability of SSH

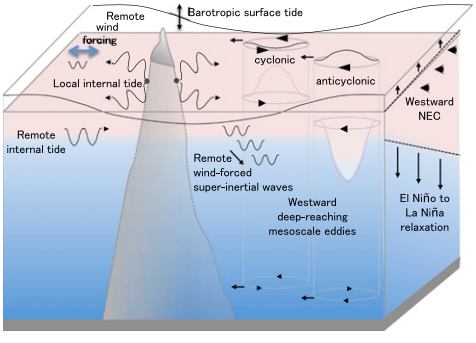

FIG. 2. Schematic of the processes examined here that affect the sea surface and pycnocline depth near Palau. Processes occur at time scales ranging from tidal (barotropic and internal), to superinertial, to mesoscale, to interannual ENSO events.

TABLE 1. PIES array details.

Site ID	Instrument type	Latitude (N)	Longitude (E)	Depth (m)[a]	$\langle c \rangle$ (m s^{-1})[b]
F1	RPIES	7°29.487′	133°47.896′	1628	1492
F2[c]	PIES	7°54.247′	133°56.502′	4438	1502
F3	CPIES	8°14.978′	134°19.887′	4283	1500
F4	RPIES	8°34.481′	133°46.686′	2395	1492
F5	CPIES	8°57.029′	134°19.839′	4157	1500
F6	PIES	8°45.019′	134°38.667′	2415	1492
F7	CPIES	8°54.009′	134°59.924′	3054	1494
F8	CPIES	8°15.318′	135°00.005′	2621	1493
F9	PIES	7°29.234′	135°30.282′	2871	1493

[a] Depths are calculated from each instrument's average pressure with mean atmospheric pressure (10.1325 dbar) subtracted, except at F2 where the depth was estimated from the ship's echo sounder.
[b] Vertically averaged sound speeds are calculated at each site from the water properties as measured during the hydrographic casts at deployment and recovery.
[c] The PIES at site F2 could not be recovered, likely due to a faulty communications board.

variations are summarized in section 4. We conclude with topics of ongoing research (section 5).

2. Data processing and interpretation

In this section, we describe the data sources and methods used in our analysis of the SSH variability observed and inferred around Palau. These include in situ data from the FLEAT program and several publicly available regional and global datasets.

a. Inverted echo sounders

As part of the FLEAT program, nine pressure-sensor equipped inverted echo sounders (PIESs) were deployed from the Research Vessel (R/V) *Roger Revelle* in May 2016 surrounding Velasco Reef off the northern tip of Palau (Table 1). Two PIESs were able to sample in "rapid mode" (RPIESs), and four of the PIESs were further equipped with near-bottom current sensors (CPIESs). The four CPIESs, two RPIESs, and two of the three standard PIESs were successfully recovered 10 months later, in April 2017, giving 314-day duration records at eight sites.

The four CPIESs were deployed underlying two repeat tracks maintained during October 2015–January 2018 with Spray underwater gliders (Zeiden et al. 2019) on either side of the meridional ridge that extends north from Velasco Reef, which is part of the larger Kyushu–Palau Ridge system (Fig. 1). Minimum spacing between neighboring instruments varied from 42 km between sites F5 and F6 to 102 km between sites F8 and F9. Some of the instruments were deployed on the satellite tracks for direct comparison of satellite-measured SSH and PIES-inferred SSH (Fig. 1b).

The C/R/PIESs (collectively referred to as PIESs hereafter, Fig. 3), were programed to obtain hourly measures of 1) bottom-to-surface, round-trip acoustic travel time $\tau(t)$; 2) bottom pressure $p(t)$; and 3) in the case of each of the four CPIESs, hourly near-bottom horizontal currents $u(t)$ and $v(t)$. The currents are not considered here for our analysis of SSH but are reported elsewhere in a study of the deep structure of mesoscale eddies (Andres et al. 2019). For our study, PIESs' bottom pressure and acoustic travel time signals provide information about mass-loading and steric changes in the overlying water column. Processing of these p and τ measurements follows established procedures and is outlined in the appendix.

1) PRESSURE RECORDS

In contrast to the current-induced blowdown of tall moorings, a PIES rests in a rigid stand (Fig. 3) that prevents contamination of the pressure record from vertical instrument motions. This, together with a precise internal instrument clock, allows us to accurately identify the amplitude and phase of the barotropic tide at each site using the response method of Munk and Cartwright (1966). This tidal contribution $p_{\mathrm{BT\_tide}}$ is the dominant signal in the pressure records, and we remove it so that we can identify other signals in the pressure records [see Eq. (1), below]. In addition, we use $p_{\mathrm{BT\_tide}}$ at each site to apply a pathlength correction to the hourly acoustic travel time records to isolate the internal tides around Palau [section 2a(2)].

For each PIES site, the residual, hourly, detided bottom pressure time series $p'(t)$ is calculated by removing the instrument drift, the barotropic tide, and the record's time-mean pressure $\overline{p}$:

$$p'(t) = p_{\mathrm{B\_meas}}(t) - p_{\mathrm{drift}}(t) - \overline{p} - p_{\mathrm{BT\_tide}}(t). \quad (1)$$

Low-pass-filtered pressure records $p'_{\mathrm{LP}}(t)$ are generated for each site by passing these hourly $p'(t)$ records

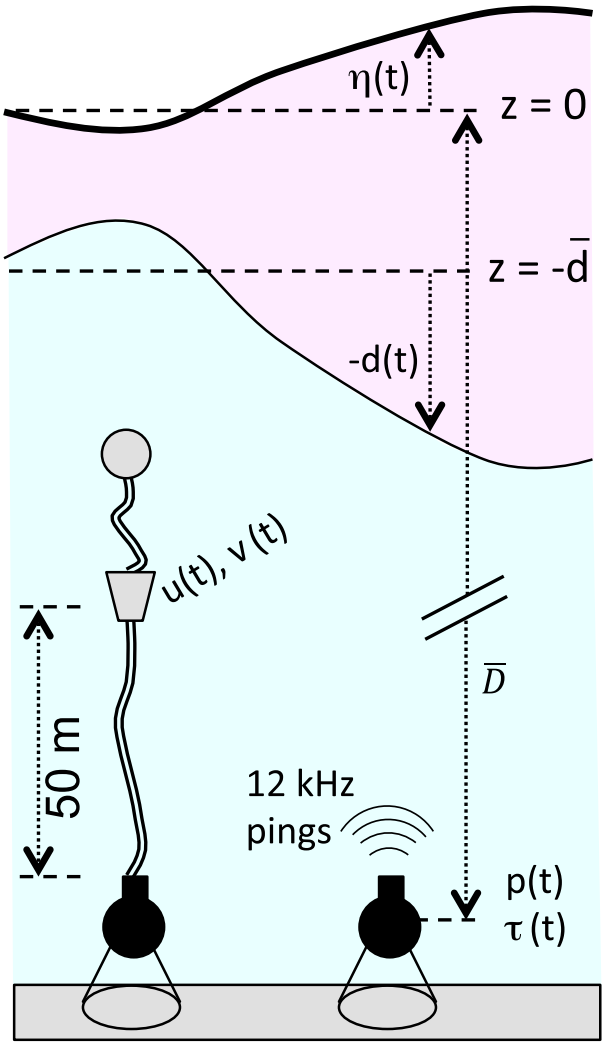

FIG. 3. Schematic of a CPIES (left side) and a PIES (right side). A C/PIES detects each 12-kHz ping's echo off the sea surface (heavy black curve), which is at $\eta(t)$. It does not detect the weaker echoes from the pycnocline (thin black curve); however, pycnocline displacements $d(t)$ do influence echoes' round-trip travel time τ via the dependence of the sound speed profile $c(z, t)$ on temperature and salinity profiles. Figure not to scale (i.e., η is typically tens of centimeters while d is tens of meters; e.g., Gill and Niiler 1973). The total (time varying) distance between the C/PIES and the sea surface is $D(t) = \overline{D} + \eta(t)$.

through a fourth-order Butterworth filter run forwards and backward with a 3-day cutoff period. (See Fig. A1 in the appendix for an example record.)

We use the hydrostatic equation, which relates $\overline{p}$ to the mean water depth $\overline{D}$, with a time-mean density profile above the instrument $\overline{\rho}(z)$ to estimate $\overline{D}$:

$$\overline{p} = \overline{p}_{\text{atm}} + \int_{-\overline{D}}^{0} \overline{\rho} g \, dz . \qquad (2)$$

Here $\overline{p}_{\text{atm}}$ is the contribution from the local time-mean atmospheric pressure, g is the acceleration due to gravity, and $\overline{\rho}(z)$ is estimated from in situ hydrographic casts [see section 2b(1)].

2) ACOUSTIC TRAVEL TIME RECORDS

The hourly measured τ depends both on the time-varying pathlength $D(t)$ between the fixed PIES and the free sea surface η (Fig. 3) and on the intervening sound speed profile $c(z, t)$. For a vertically averaged sound speed $\langle c \rangle$ this dependence is

$$\tau(t) = 2\int_{-\overline{D}}^{\eta(t)} 1/c(z,t)\, dz = 2D(t)/\langle c \rangle , \qquad (3)$$

where the factor of 2 arises because the measured time interval is a round-trip travel time. Typically, most τ variability is due to changes in the sound speed profile, which in turn is sensitive to temperature (and to a lesser extent, salinity) in the water column overlying the instrument. Because of the strong temperature dependence of c, τ often serves as an excellent proxy for thermocline and pycnocline displacement in many regions. However, pathlength changes can also measurably influence τ, and in conjunction with bottom pressure measurements can be used to infer mass-loading changes in the overlying waters.

Spectral analysis of the hourly τ measurements from the FLEAT PIES array shows that most of the variance is at tidal periods (Fig. 4a). Much of this is coherent with bottom pressure variability, indicating that pathlength changes associated with barotropic tides dominate the τ signal here. However, the phase of individual tidal constituents in the τ records is nonstationary, with this variability arising from internal tides. The barotropic (τ_{BT}) and internal (or "baroclinic," τ_{BC}) tidal signals can be separated from the full τ signal using the method described in the appendix that capitalizes on the PIESs' collocated measures of travel time and bottom pressure.

Spectra of the barotropically detided hourly records $\tau - \tau_{\text{BT}}$ still have tidal energy at diurnal and semidiurnal periods (e.g., Fig. 4b). This internal tidal signal τ_{BC} manifests in τ because the first mode internal tide can cause vertical isopycnal motions that affect τ via changes in the vertically averaged sound speed [i.e., via $\langle c \rangle$ in Eq. (3)] rather than due to changes in pathlength. There may also be higher mode internal tides, however, these likely do not manifest so clearly in τ, since isopycnal shoaling—and decreases in sound speed—at some depths may be compensated by isopycnal deepening—and increases in sound speed—at other depths (e.g., Li et al. 2009). To isolate τ_{BC}, we apply bandpass filters to the barotropically detided records τ_{BT} at 23.0–26.8 h for the

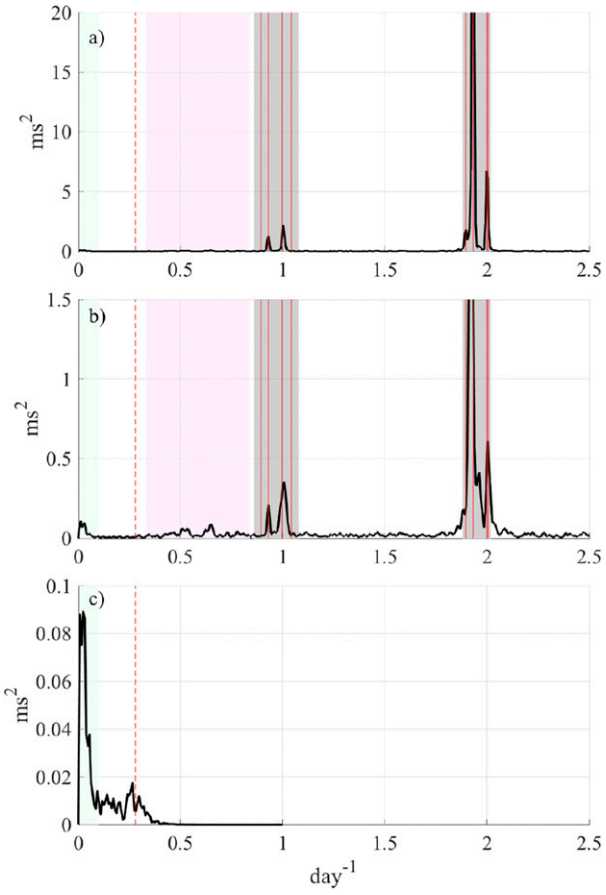

FIG. 4. Example spectra of acoustic travel times from site F8. (a) Variance preserving spectrum of τ (i.e., the full hourly acoustic-travel-time record) at site F8. (b) Variance preserving spectrum of τ_{BT} (i.e., the "detided" acoustic-travel-time record, which is the hourly record with the contribution from the barotropic tide removed). (c) Variance preserving spectra for 3-day low-pass-filtered τ'_{LP}). In each panel, the local inertial frequency is denoted with the red dashed line; the frequencies used in the response method detiding (Munk and Cartwright 1966) are shown with solid red lines (from low to high frequency, these are diurnal: Q1, O1, P1, K1, and semidiurnal: N2, M2, S2, K2). The gray shaded bands are the frequency bands used here to bandpass filter the internal tide's contribution to acoustic travel time. The mesoscale band (green) and a superinertial band (pink) are also indicated. Note the different vertical scales in the panels.

diurnal internal tide τ_{D1} and at 11.50–12.92 h for the semidiurnal internal tide τ_{D2} following Park and Watts (2006). The amplitudes of the diurnal and the semidiurnal internal tides identified in this way each vary independently (e.g., Fig. A2 and Table 2), both over time and from site to site, and are considered further in section 3a.

With these barotropic and internal tide contributions to the hourly acoustic travel time records quantified, we are able to calculate a residual hourly record τ', that captures temporal perturbations to travel time arising from nontidal processes (e.g., Fig. A2, red curve):

$$\tau'(t) = \tau(t) - \tau_{BT}(t) - \tau_{BC}(t) - \overline{\tau}. \quad (4)$$

The $\overline{\tau}$ at each site depends on $\overline{D}$ and on the time-averaged, vertically averaged sound speed at the site $\overline{c}$:

$$\overline{\tau} = 2\overline{D}/\overline{c}. \quad (5)$$

A low-pass-filtered record τ_{LP} is formed from the hourly τ using a fourth-order Butterworth filter run forwards and backward with a 3-day cutoff period. From this, $\overline{\tau}$ is removed to obtain a low-passed, demeaned record τ'_{LP} at each site (e.g., Fig. A2, gray curve). Variance preserving spectra of τ'_{LP} (Fig. 4c) show that most of the variance in τ'_{LP} occurs at periods between about 20 and 100 days; based on the spectra, this range is used here to isolate the "mesoscale band" with 10 days used as a cutoff period for further filtering to obtain $\tau'_{10\text{-d\_LP}}$. To explore the mesoscale band, these low-pass-filtered records are examined in section 3c with lagged-correlation analysis and complex empirical orthogonal function (CEOF) analysis (Horel 1984). Separately, the hourly records are detided and then bandpass filtered between 1 and 10 days to isolate nontidal, high-frequency variability τ'_{BP}, including a superinertial signal, using lagged correlations and CEOF analysis (section 3d).

TABLE 2. Acoustic travel time variance (ms^2).

Site ID	Tidal			Superinertial	Mesoscale
	τ_{BT}	τ_{D2}	τ_{D1}	τ_{BP}	$\tau_{10\text{-d\_LP}}$
F1	0.348	0.077	0.064	0.068	0.209
F3	0.334	0.088	0.064	0.067	0.225
F4	0.343	0.111	0.051	0.059	0.293
F5	0.325	0.102	0.123	0.069	0.283
F6	0.326	0.104	0.028	0.069	0.310
F7	0.314	0.063	0.020	0.069	0.389
F8	0.310	0.046	0.017	0.056	0.289
F9	0.296	0.030	0.013	0.039	0.283

3) INTERPRETING ACOUSTIC TRAVEL TIME

Acoustic travel time records have been used in conjunction with historical hydrography to successfully infer the temporal variability of the low mode vertical structure in the ocean in many regions (e.g., Meinen 2001; Donohue et al. 2010). The gravest empirical mode (GEM) method constructs a lookup table of acoustic travel times at some reference pressure τ_{ref} associated with historical vertical profiles of temperature and salinity. Near Palau, where the pycnocline is shallower than 200 m (Schönau and Rudnick 2015),

we choose 990 dbar as the reference level as this allows us to use data from the many (>7000) Spray glider dives in the region to construct the GEM lookup table for τ_{990} (see the appendix for method details and error analysis). To enable quantification of errors in pycnocline depth, a second lookup table is constructed directly relating τ_{990} to the depth of the 1024.5 kg m^{-3} pycnocline, using the same principle (Tracey et al. 1997). We only convert τ to τ_{990} at those instrument sites where we have concurrent Spray glider data from nearby dives (within a 10-km box around a given PIES site), as a comparison to calibration using regional historical hydrography at these sites gives little confidence in its utility in this region (see the appendix). Using concurrent Spray data to construct regression parameters for calibration, we are able to calibrate each of the 4 CPIESs (located at sites F3, F5, F7, and F8, which are near the repeat glider tracks).

For these four CPIESs, τ_{990} and the lookup tables allow estimation of the time series at each CPIES site of temperature, salinity and specific volume anomaly profiles: $T(z)$, $S(z)$, and $\delta(z)$, respectively, and the integrated quantity, geopotential anomaly ϕ:

$$\phi = \int_0^p \delta \, dp. \tag{6}$$

Using a dedicated lookup table, we also estimate at each of these four sites the time-varying depth of the thermocline (or pycnocline, here defined by the 1024.5 kg m^{-3} potential density surface) d.

For the other PIES sites we are unable to calibrate in situ measurements to obtain time series of τ_{990}, as historical hydrography in the region does not capture local deep variability in travel time (see the appendix, Fig. A4). Nevertheless, we do make use of all of the travel time records to track signal propagations across the array in various frequency bands.

4) Using τ_{990} and P' to diagnose mass-loading and steric contributions to SSH

From p and τ_{990}, we can estimate the total SSH at each site (neglecting the inverted barometer effect), as well as the various contributions to the overall SSH signal. The total sea surface height signal at each site, η, is a function of both the steric (related to τ) and mass-loading (related to p) contributions:

$$\eta = \eta_{BT} + \eta_{BC} + \eta_{ST} + \eta_{ML}. \tag{7}$$

The first two terms on the right hand side of Eq. (7) are the tidal contributions [from the barotropic and internal tides, respectively, discussed in section 3a]; η_{ST} is the (nontidal) steric signal, and η_{ML} is the (nontidal) mass-loading signal (e.g., Baker-Yeboah et al. 2009), where

$$\eta_{ST} = \phi/g, \quad \text{and} \tag{8}$$

$$\eta_{ML} = p'/\rho_B g. \tag{9}$$

Here g is acceleration due to gravity, ρ_B is bottom density, ϕ is obtained from Eq. (6), and τ_{990} interpreted with the GEM lookup table for specific volume anomaly $\delta(z)$. The mass-loading and steric signals associated with the mesoscale band are considered further in section 3c.

b. Other data

Additional datasets and model output are used to help interpret the PIES observations and to provide spatial and temporal context for the FLEAT experiment.

1) Hydrography

Temperature and salinity profiles from various sources taken in the region around Palau are used here in several ways. Some profiles are used to estimate $\langle c \rangle$ at each instrument site, which is used to calculate the barotropic tide's contribution to acoustic travel time [τ_{BT}, see section 2a(2)]. Temperature and salinity profiles are also used to convert acoustic travel times measured at the four CPIES sites to their reference values τ_{990} (see the appendix). Finally, the hydrographic data are used to build the lookup tables from which the time-varying vertical profiles of temperature, salinity or specific volume anomaly can be inferred from τ_{990} [see section 2a(3) and the appendix].

The hydrographic profiles used here include shipboard measurements from full-water column CTD casts taken at each PIES site after deployment and again before recovery with the R/V *Revelle*'s standard Seabird system and deep casts from 85 WOCE sites from the period 1989–2010. In addition, profiles that were measured during the experiment period around Palau and that reach to at least 990 dbar are used here. These comprise 26 casts from the FLEAT cruises (including the aforementioned full-water column casts) and a subset of 7000 profiles measured close to Palau during the experiment period with Spray gliders as part of the FLEAT program (Zeiden et al. 2019). Of these 7000 glider profiles, 186, 120, 147, and 139, respectively, were taken within one hour of a CPIES travel time measurement, and within 11 km of sites F3, F5, F7, and F8.

In addition, hydrographic profiles from Argo floats in the region 4°–11°N and 131°–138°E from 2002 onward are used to compute a time series of the region's area-averaged thermocline depth, which is then compared

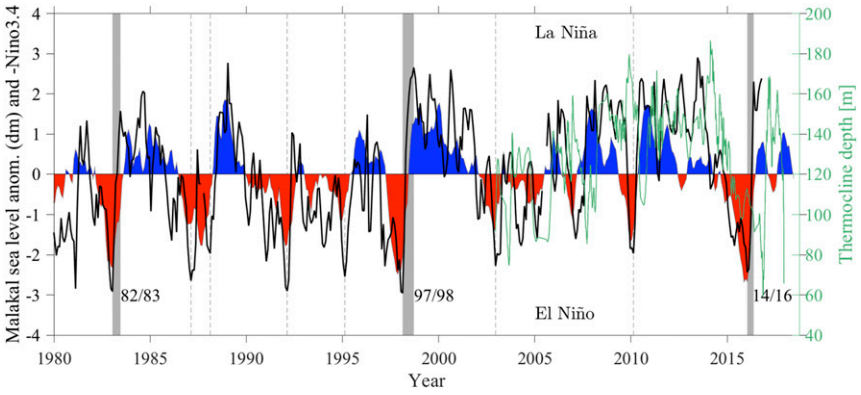

FIG. 5. Monthly mean sea level anomalies measured by the tide station at Malakal, Palau (black) and an ENSO indicator (plotted as the inverse of the Niño-3.4 index) showing El Niño (red) and La Niña (blue) periods. Depth of the 1024.5 kg m^{-3} isopycnal (i.e., the thermocline), calculated from Argo profiles in the region of Palau, is plotted in green from 2002 onward. Transitions at the ends of ''very strong'' El Niño events (1982/83, 1997/98, and 2014/16) are shaded; these correspond to large sea level increases at Palau. The minimum sea levels associated with the ''strong'' and ''moderate'' El Niño events (1986/87, 1987/88, 1991/92, 1994/95, 2002/03, and 2009/10) are denoted with dashed lines; as with the very strong events, these El Niño events are also followed by marked sea level increases at Malakal.

to tide gauge measurement and the Niño-3.4 index (section 3b). Argo float profiles with salinities less than 30 psu or more than 40 psu are discarded, as are profiles with fewer than five pressure measurements, leaving a total of 2693 profiles over the period.

2) SPRAY GLIDER DIVES

In addition to using salinity and temperature profiles from glider casts to interpret the CPIESs' τ_{990}, we use glider data to estimate the mesoscale spatiotemporal variability of the pycnocline depth around Palau. Individual profiles, collected over about 3 h, are obtained by binning in situ glider data at 10-m increments in the vertical, after which data are objectively mapped to a regular grid in time and latitude to obtain time series of water properties along two sections that cross the NEC north of Palau. These meridional sections are on either side of the ridge along a ''west line'' at 134.25°E and an ''east line'' at 135°E (see Fig. 1a). The objective map is created using a 14-day by 30-km Gaussian decorrelation scale following Zeiden et al. (2019). To obtain Hovmöller diagrams of pycnocline depth anomaly as a function of latitude and time, we linearly interpolate depth as a function of density to constant density surfaces, with a focus here on the 1024.5 kg m^{-3} isopycnal (as a proxy for the pycnocline). Anomalies are calculated with respect to a constant time-latitude mean depth over the 10-month CPIES deployment period. We discuss the characteristics of the large-scale pycnocline variability in section 3c.

3) TIDE GAUGE DATA

Due to strong interannual variability in the tropical North Pacific associated with El Niño events (Wang et al. 2019; Andres et al. 2019), long-term tide gauge data are used here to provide temporal context for the 2016–17 FLEAT experiment period. Sea level observations since 1969 are available from a tide station maintained at Malakal on Palau (7.333°N, 134.467°E, GLOSS ID 120). Both the annual-mean and the monthly mean Revised Local Reference (RLR) sea levels were obtained from the Permanent Service for Mean Sea Level (PSMSL 2018; Holgate et al. 2013) for the period from 1980 through 2018 (Fig. 5, black curve).

4) NIÑO-3.4 TIME SERIES

To identify El Niño-to-La Niña transition events, the monthly Niño-3.4 index (Fig. 5, red and blue shaded curve) was downloaded from the NOAA Climate Prediction Center to examine the period from 1980 through mid-2018 (L'Heureux et al. 2013; NCEP/NOAA 2018). This index is related to SST anomalies in the region 5°N–5°S, 120°–170°W.

5) WIND STRESS

To examine possible mechanisms underlying 1.1–3.0-day variability identified in the PIES measurements, wind stress reanalysis data across the Pacific from the equator to 39°N were downloaded spanning 2015 through the end of 2017 (Kalnay et al. 1996; NCEP 2018).

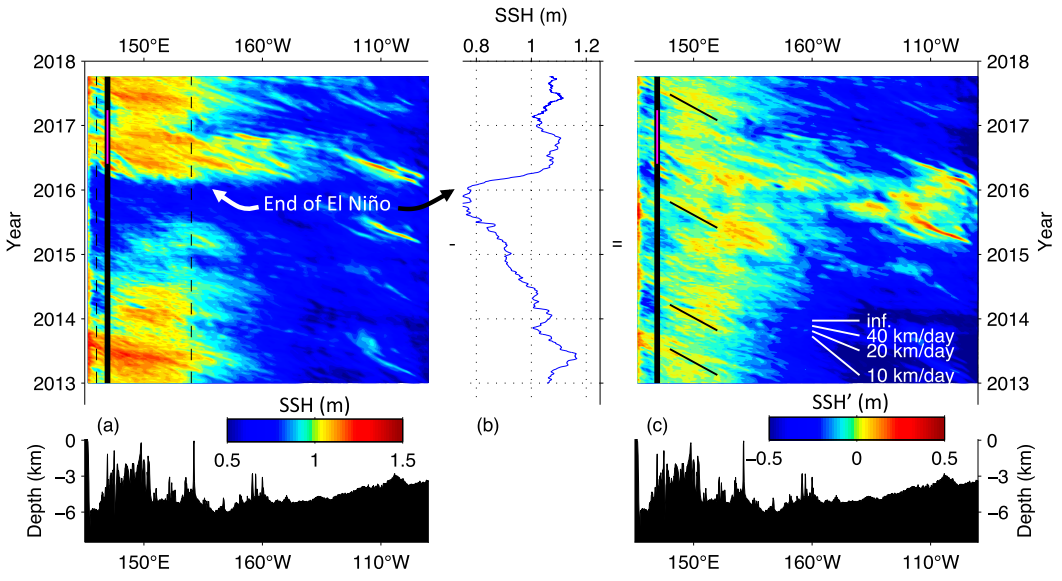

FIG. 6. (a) Time vs SSH_{sat} (meridionally averaged over 8°15′–8°45′N). The longitude of Palau is indicated with the solid black line, and the time period during which the array was deployed (2016–17) is highlighted in magenta on this line. Topography along the Pacific is indicated in the lower subpanel. (b) Time series of SSH_{sat} zonally averaged between the black dashed lines shown in (a). (c) Time vs SSH'_{sat}; black phase lines show westward propagation at 15 km day^{-1}; several other propagation speeds are shown for comparison (white lines). Topography along the Pacific is indicated in the lower subpanel.

NCEP reanalysis daily averages of the zonal and meridional components of the momentum flux are available at 1.9° spatial resolution. From these data, the daily wind stress curl is calculated. On average, the curl in the tropical North Pacific is positive both during El Niño and La Niña periods.

6) SATELLITE SSH

Measures from satellite altimetry of SSH across the North Pacific spanning 5°–20°N from 2013 through the second half of 2017 were obtained from the mapped absolute dynamic topography (MADT) daily product, which is available at ¼° resolution from the Copernicus Marine Environment Monitoring Service (CMEMS 2017). Though the product is provided at daily intervals, the individual satellite reference tracks (Fig. 1b) are only repeat sampled at about 10-day intervals.

SSH from altimetry is used here to compare directly with the in situ measurements during the FLEAT experiment (section 3c) and further to provide spatial context for the region around Palau by highlighting westward-propagating signals.

To identify these large-scale propagating signals, we meridionally averaged MADT over the latitude band 8°15′–8°45′N to obtain SSH_{sat}. A Hovmöller plot of SSH_{sat}, shows variability superimposed on a general east–west gradient, with lower SSH_{sat} toward the eastern half of the basin (Fig. 6a). Slopes of the phase lines on this plot indicate that some of this variability is either propagating very rapidly across the entire basin (e.g., as barotropic Rossby waves; Andres et al. 2012) or it is associated with large-scale zonal processes like seasonal heating and cooling. One particularly striking feature that stretches across much of the western basin, is a broadscale SSH_{sat} increase by about 30 cm in early 2016. As discussed in section 3b, this is associated with a rapid transition from El Niño to La Niña, which occurred just before the FLEAT PIES array deployment; the transition was already complete by May 2016 when the PIESs were deployed (Schönau et al. 2019).

To highlight that part of SSH_{sat} that may be associated with slow westward-propagating mesoscale eddies, we filter SSH_{sat} as follows. At each time, SSH_{sat} is averaged over a zonal band stretching from 130° to 170°E (Fig. 6b). This zonally uniform SSH time series is subtracted from the full SSH_{sat} at each longitude and time to give a residual SSH'_{sat} (Fig. 6c). The sloped phase lines of signals that approach the longitude of Palau suggest signal propagations of about 15 km day^{-1} toward the west. During the instrument deployment period (2016–17), a series of about five sea surface highs and lows reaches Palau. Their amplitude in SSH'_{sat} spans from about −11 to +5 cm.

7) NUMERICAL MODEL OUTPUT

Measurements of the barotropic tide from bottom pressure from the FLEAT PIES array are compared to

TABLE 3. Barotropic tide amplitude (first number) and phase (second number).

Site ID	Tide amplitude (dbar) and phase (°)															
	O1		K1		Q1		P1		M2		K2		N2		S2	
F1	0.133	62.73	0.193	76.59	0.027	57.37	0.063	75.71	0.522	292.11	0.059	326.34	0.099	277.51	0.220	323.58
F3	0.132	61.05	0.194	76.81	0.027	56.33	0.063	75.69	0.519	292.08	0.058	326.24	0.098	277.45	0.217	323.45
F4	0.132	62.02	0.193	76.48	0.026	56.03	0.063	75.59	0.522	292.04	0.059	325.93	0.099	277.70	0.219	323.17
F5	0.135	60.95	0.187	76.19	0.028	54.84	0.062	75.24	0.511	292.19	0.057	326.04	0.097	277.76	0.212	323.28
F6	0.134	59.24	0.198	73.55	0.026	54.92	0.065	72.50	0.501	291.34	0.055	324.19	0.097	276.36	0.206	321.66
F7	0.133	59.17	0.196	73.41	0.026	54.84	0.064	72.39	0.495	291.89	0.054	325.36	0.095	276.75	0.202	322.69
F8	0.133	58.91	0.198	73.37	0.027	54.64	0.065	72.33	0.489	291.50	0.053	325.47	0.095	276.34	0.197	322.77
F9	0.134	58.75	0.201	73.37	0.026	53.83	0.066	72.36	0.478	291.18	0.051	324.93	0.093	275.64	0.190	322.28

the output of TPXO7.2, a 0.25° global tide model constrained to best fit the Laplace tidal equations and altimetry data (Egbert and Erofeeva 2002).

To further examine the source of the ''superinertial'' signal identified in the FLEAT observations (section 3d), we use output for the region 6°–16°N, 123°–137°E from an eddy-resolving numerical model. The output, available at 3-h interval, is from a data-assimilated Hybrid Coordinate Ocean Model (HYCOM) as described in Chassignet et al. (2007).

3. Results and discussion

The acoustic travel time records from each PIES site have energy in several frequency bands indicative of a wide range of processes contributing to the overall surface and subsurface variability around Palau (section 2, Table 2 and Fig. 4). Based on the datasets and methods described in section 2, we examine variability in SSH and pycnocline depth d near Palau at tidal (diurnal and semidiurnal), superinertial (1.1–3.0 days), mesoscale (20–100 days), and interannual time scales. For these bands, we consider the amplitudes of the signals, their propagation across the PIES array, and their predictability. We begin with the largest (and most predictable) contributor to SSH variability, the barotropic tide.

a. Tidal variability

We determine the amplitudes and phases of eight tidal constituents of the barotropic tide by applying the response method to the observed pressure records p from each PIES site (Table 3). With this, we then identify the internal tides from p and τ as described in section 2a(2).

1) BAROTROPIC TIDES

The largest tidal constituent, the M2 tide, has amplitude and phase that each increase slightly from east to west across the array (by about 4 cm and 1°). For the K1 tide, which is the most energetic of the diurnal constituents, amplitude varies little within the array (~1 cm) and the phase increases by about 3° from east to west. As an example, the total barotropic tide at F8 leads to a standard deviation in η_{BT} of about ±42 cm and a maximum range at spring tide of about ±1 m (Fig. A1a); this translates to a variance in travel time (i.e., in τ_{BT}) of about 0.31 ms^2 due to pathlength changes as the sea surface rises and falls. The standard deviation of η_{BT} is similar at the other sites (Table 2).

The observed tides from the FLEAT PIES sites generally compare well with the amplitudes and phases modeled by the TPXO7.2 global inverse barotropic tidal solution (Egbert and Erofeeva 2002), though amplitude is slightly larger in the observations than in the model output, both for the K1 tide (Fig. 7a) and for the M2 tide (Fig. 7c). For the K1 tide, the phasing around the complicated bathymetry surrounding Palau is reproduced well by the model (Fig. 7b) and for the M2 tide, the model suggests some structure in the phase that is not borne out by the observations (Fig. 7d). We note that the model bathymetry is relatively coarse at the scales of the island, with a shallowest point of around 100 m—thus the island of Palau is represented in this model as a seamount. These small discrepancies between modeled and PIES-observed barotropic tides, suggest that it is necessary to have local measures of barotropic tides to properly isolate the internal tides in the acoustic travel time records.

2) INTERNAL TIDES

Using thermistor data and a numerical model, Wolanski et al. (2004) inferred that internal tides are generated on the slope of the island and radiate outwards into the ocean interior. Observations from the PIES array confirm the presence of internal tides around the island, and show that, in general, the semidiurnal internal tides near Palau reach larger amplitudes than do the diurnal tides (Fig. 8, cf. the left and right columns), with the exception of site F5 where the diurnal tide is particularly enhanced. The diurnal internal tides observed by the FLEAT PIESs are relatively strong compared to

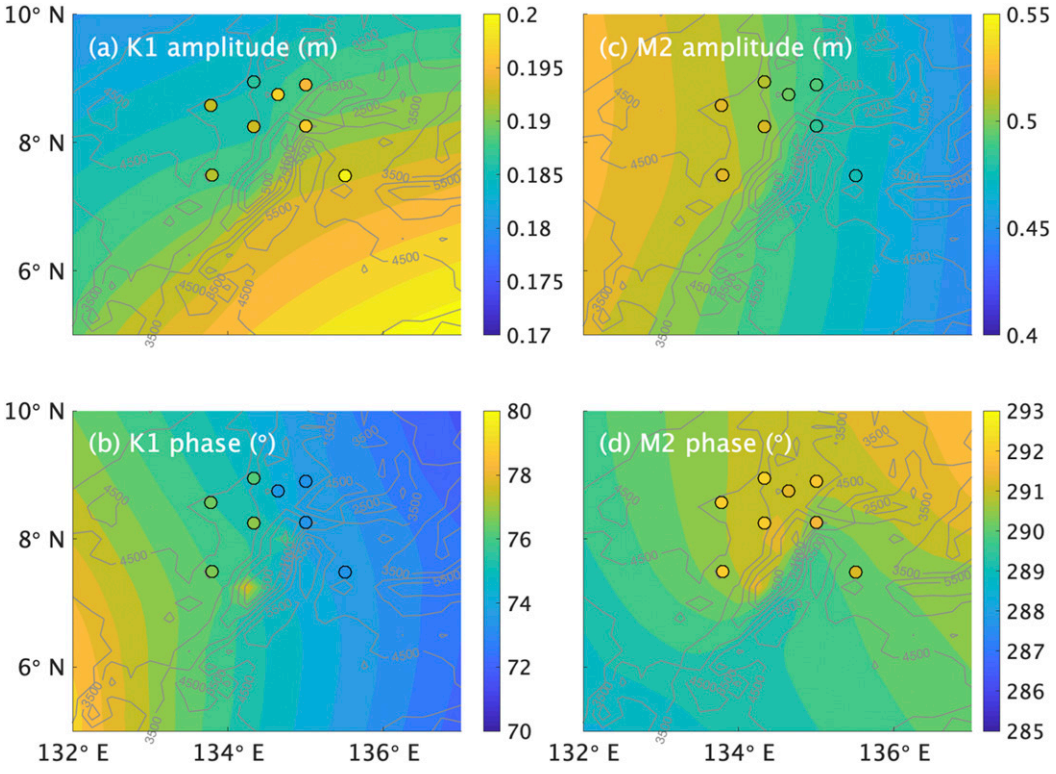

FIG. 7. (a),(c) Amplitude and (b),(d) phase of the (left) diurnal K1 tide and (right) semidiurnal M2 tide as calculated with the response method (Munk and Cartwright 1966) applied to the in situ pressure records from the PIES sites (colored dots) and as estimated in the region (shading) from a global tidal model (Egbert and Erofeeva 2002). Bathymetric contours are shown with a 1000-m interval from 500- to 5500-m depth.

the diurnal signals observed in other PIES experiments; this is consistent with recent high-resolution HYCOM model runs that incorporate tidal forcing (e.g., Arbic et al. 2012). The 1/25° HYCOM simulations suggests that Palau in the western tropical North Pacific, sits in a region of particularly strong diurnal internal tides, in addition to strong semidiurnal internal tides there (Savage et al. 2017, see their Figs. 14 and 15).

The pycnocline (or thermocline) displacements d associated with internal tides at sites F3, F5, F7, and F8 are inferred here using both the GEM and a direct empirical relation between τ and thermocline depth (Fig. 8, red y axes on the right), with negligible differences from each method. The vertical structure of the internal tide contributing to the travel time variability cannot be unambiguously identified using these data, but the structure of the GEM suggests that they are dominantly mode 1 (Fig. A6). We note that the contributions of higher modes to travel time variability (discussed by Li et al. 2009) are sensitive to both the amplitudes of the modes and their structure (derived from the stratification profile), but they are expected to be small, perhaps contributing to the scatter in these estimates. Internal tides are estimated here to have pycnocline (thermocline) displacement amplitudes of around 5 m at the eastern sites (F7 and F8) and 10 m at each of the western sites (F3 and F5).

An estimate of the SSH anomaly associated with these pycnocline displacements can be made by assuming the vertical structure of the internal tide is that of a mode 1 wave over a flat bottom. Full depth CTD casts from the PIES deployments and recoveries are used to form stratification profiles at each of the sites, which are then used to numerically solve the linear internal wave eigenvalue problem for waves at tidal frequencies. By varying the amplitude of the computed mode 1 structure, a relation between travel time anomalies associated with the modes and their SSH is derived, with a 1-ms anomaly in travel time being associated with around 5-cm SSH anomaly at each of the sites. As such, internal tide SSH anomalies are estimated to lie in the range of 2–5 cm at each location, covarying in time with the amplitudes of isotherm (and isopycnal) displacements.

Overall, τ_{D1} and τ_{D2} amplitudes are smaller on the eastern side of the island compared to the west, though

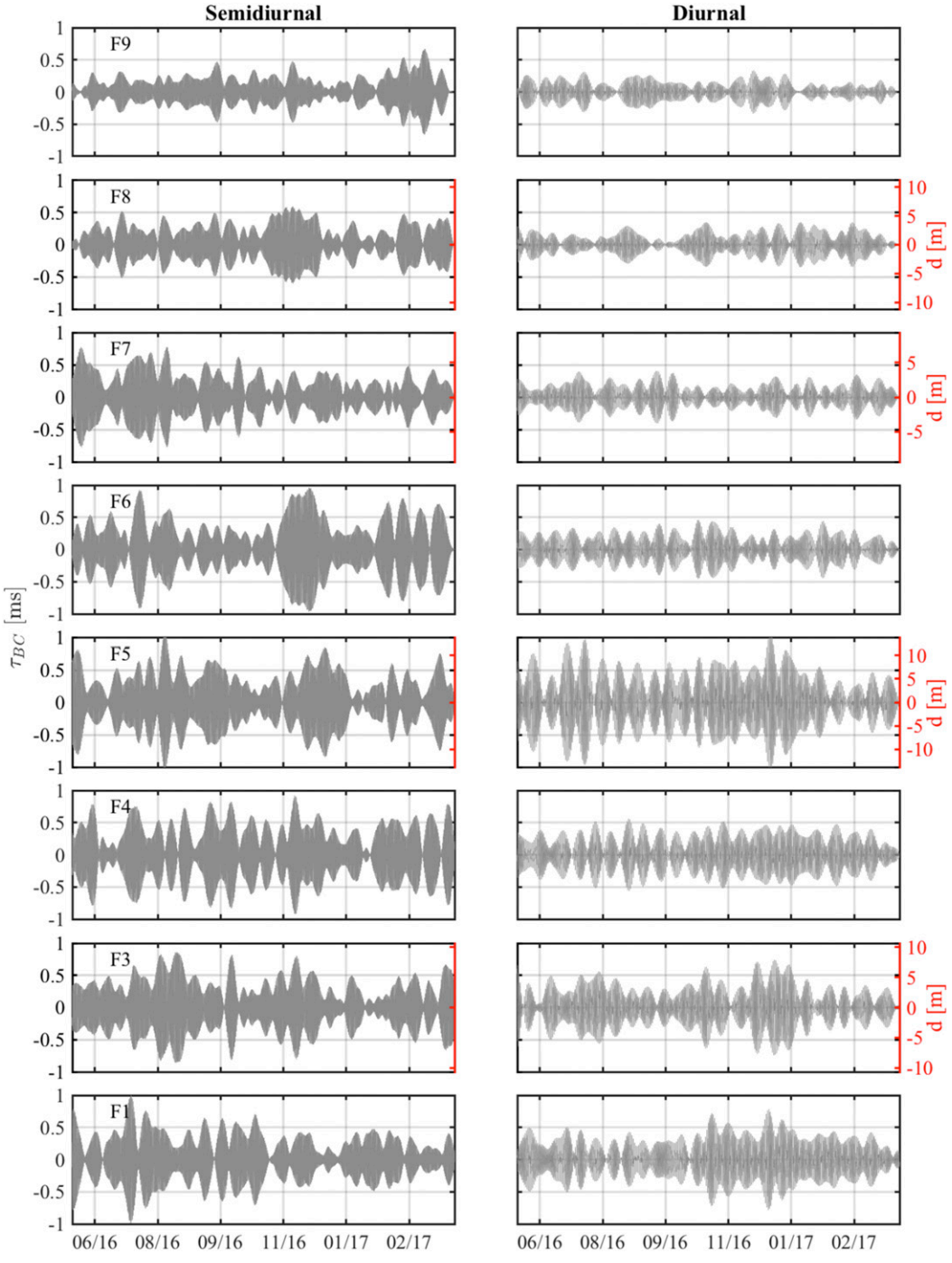

FIG. 8. Time series of (a) the semidiurnal τ_{D2} and (b) the diurnal components τ_{D1} of τ_{BC} extracted from the PIES records (black axis). Right axes (red) show the associated thermocline displacements d for the sites (F3, F5, F7, and F8) for which it is possible to calibrate the travel time measurements due to the nearby glider profiles [see section 3a(2)].

at the uncalibrated instrument sites this should be interpreted with some caution. Nevertheless, if the uncalibrated travel time amplitudes do represent the amplitude of the internal tide, it suggests the presence of relatively stronger diurnal tides to the north and west of the island compared to the east.

Temporal variability in τ_{D1} and τ_{D2} amplitude is evident at each of the sites in both tidal bands. Though some

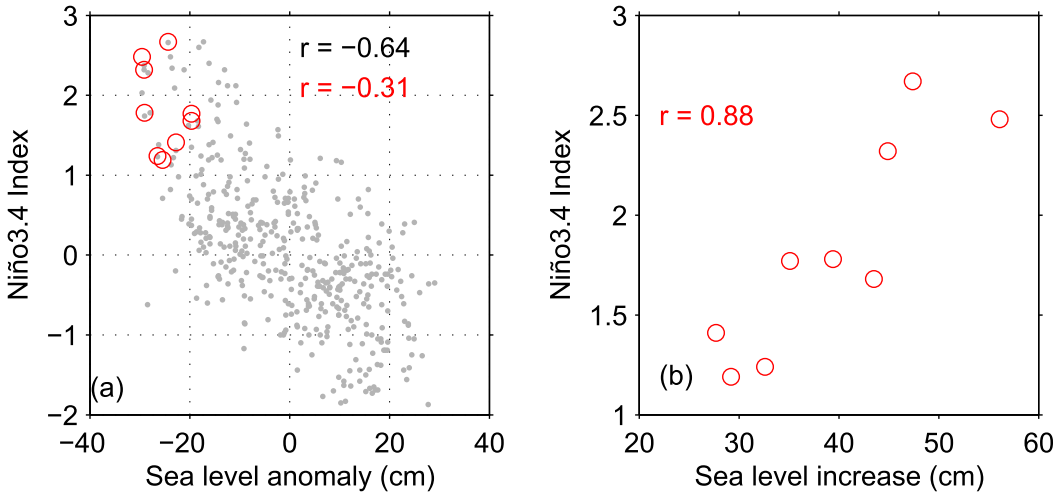

FIG. 9. (a) Monthly mean sea level anomalies from the Malakal tide station vs the contemporaneous Niño-3.4 index from 1980 through mid-2016 (gray). The minimum sea level anomalies and peak Niño-3.4 index values recorded during each El Niño event are shown by red circles (note these are usually not quite synchronous as the sea level extrema generally lag the Niño-3.4 maxima by ~2 months). (b) Sea level increase experienced at Malakal after each of the nine El Niño events (calculated as the first maximum sea level attained after the Niño-3.4 index begins to fall minus the minimum sea level experienced during the El Niño event).

of this variability in amplitude can be attributed to local changes in internal tide forcing associated with the spring-neap cycle, there is considerable variability of a more intermittent nature. This intermittency is characteristic of internal tide measurements, which are a sum of locally generated internal tides and internal tides generated remotely, the latter having traveled long distances from their generation point (Nash et al. 2012). Variability in remotely incident waves can arise from processes that influence the paths and speeds of waves as they transit from their source. In particular, mesoscale changes in stratification and currents can refract internal waves toward and away from the measurement location (Rainville and Pinkel 2006). At Palau, we likely see manifestations of both local (from the Kyushu–Palau Ridge) and remote sources. The relatively larger internal tides to the west of the island insinuate the Luzon Strait or Sangihe Ridge as potential remote source regions, with the strong mesoscale variability of the western Pacific then contributing to the observed internal tide variability of signals that arrive at Palau. The lack of consistent time variability in internal tide amplitudes across the array illustrates the lack of spatial coherence of the internal tide in this region. For example, relatively larger internal tides were observed around mid-September 2016 at site F5, but not at F6, only 40 km away.

b. *El Niño*

While the barotropic tide causes the largest amplitude SSH variability observed around Palau, SSH variability on interannual time scales also has large amplitudes here, a manifestation of the dominance of ENSO. Increases in sea level of up to 40 cm are observed at island tide gauges, with these changes associated with transitions from El Niño to La Niña (Fig. 5, gray bands and dashed lines). In general, sea level around Palau is anomalously low throughout El Niño periods (Figs. 5 and 9a), but the extrema in sea level and in Niño-3.4 index are not perfectly synchronous. For the nine El Niño events that occurred between 1980 and 2016, sea level reached a minimum at the tide gauge in Malakal on average about 2 months after the maximum in Niño-3.4 index; the lags range from 0 to 5 months. Further, the correlation between the strength of each of the nine El Niño events and the minimum sea level experienced at Malakal during that event is relatively weak (correlation $r = -0.31$). In contrast, the sea level rise experienced *after* each El Niño event is strongly positively correlated with the strength of the preceding El Niño event ($r = 0.88$, $p = 0.002$ and Fig. 9b) where strength is quantified by the maximum in Niño-3.4 index reached during the El Niño. This high correlation suggests that the Niño-3.4 index is an excellent predictor of the subsequent sea level rise that will be experienced in Palau over the following 3–7-month period. For every unit strength of a given El Niño event (i.e., as quantified by the maximum Niño-3.4 index reached during the event), there will be a 22-cm (±3-cm standard deviation) increase in sea level at Malakal (relative to the minimum attained during the El Niño, typically ~2 months after the maximum in Niño-3.4 index) as

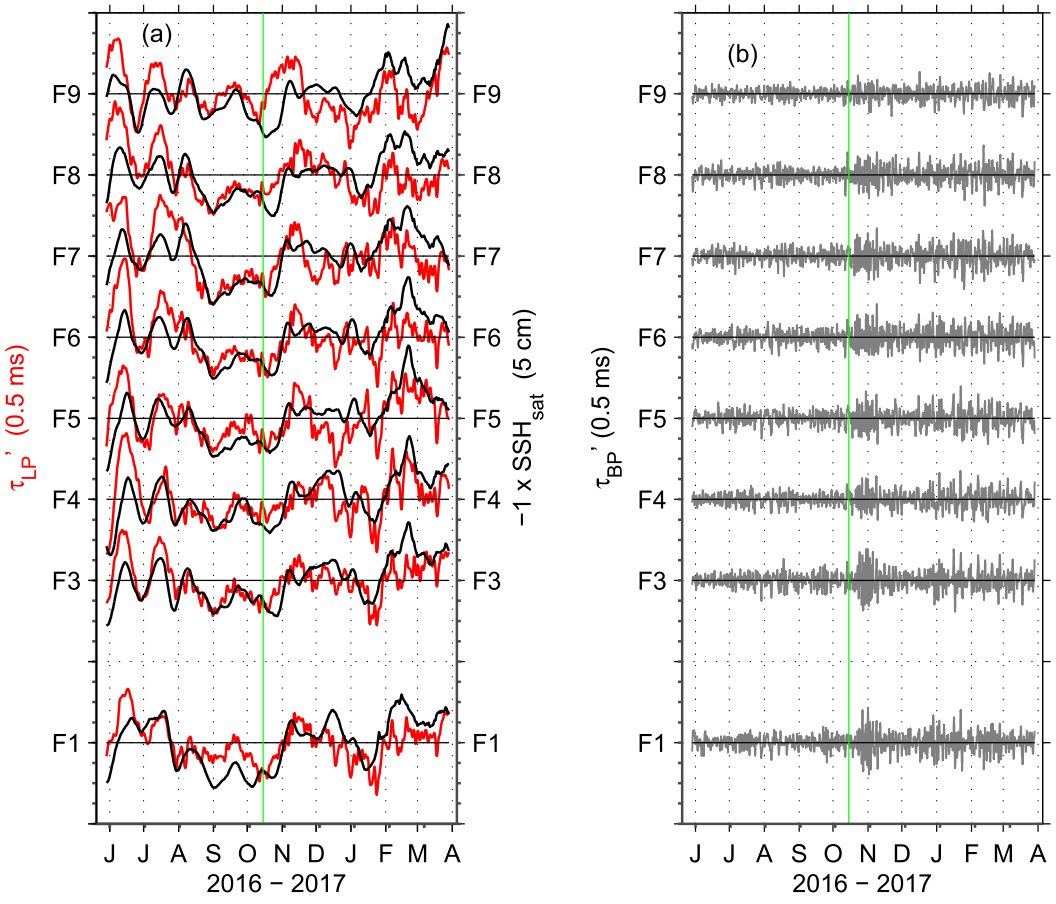

FIG. 10. (a) τ'_{LP} (red) for each PIES site superimposed on the mapped SSH_{sat} interpolated to each instrument location and demeaned (black). The interval between τ'_{LP} tick marks is 0.5 ms, and the interval between (demeaned) SSH_{sat} tick marks is 5 cm, where the SSH scale is reversed (increasing downward) to better highlight the negative correlation. (b) τ'_{BP} for each site (1–10-day band). The interval between tick marks is 0.05 ms. In both panels, the green line highlights 15 Oct 2016 when the correlation between SSH and acoustic travel times deteriorates.

the conditions around Palau relax toward the La Niña state.

The details of the processes underpinning the correlations and the observed lags remain to be investigated in a future study. In the meantime, to examine whether this striking ENSO SSH signal has a corresponding expression in the pycnocline (or thermocline) around Palau, we turn to the Argo profiles from the region. With these temperature and salinity profiles, we calculate an area-averaged time series of the depth d of the 1024.5 kg m^{-3} isopycnal since 2002 in the region surrounding Palau (Fig. 5, green line). Over periods of months to years, d varies by tens of meters, with the largest shoaling of more than 100 m associated with El Niño 2014/16. During this same period, sea level at the island tide gauge drops by 50 cm. A linear regression between SSH from the tide gauge and d from the (area-averaged) Argo floats (figure not shown) has an R^2 value of 0.51, indicating that around 50% of pycnocline variance is explained by variance in surface height, with an average of 1-cm SSH displacement at Palau corresponding to a 2.5-m pycnocline displacement (in the opposite direction) in the region.

c. *Mesoscale variability*

On the backdrop of the region's strong interannual SSH variability associated with ENSO, we next consider the influence on SSH of mesoscale eddies around Palau during the FLEAT experiment period. The 10-month duration PIES τ'_{LP} records show strong mesoscale variably at periods from 20 to 100 days (see the green shaded band in Fig. 4c). As expected, to first order, this τ'_{LP} is anticorrelated with the mapped SSH_{sat} interpolated to each instrument site (Fig. 10a), particularly during the first half of the deployment period from April to October. This sense of correlation is consistent with

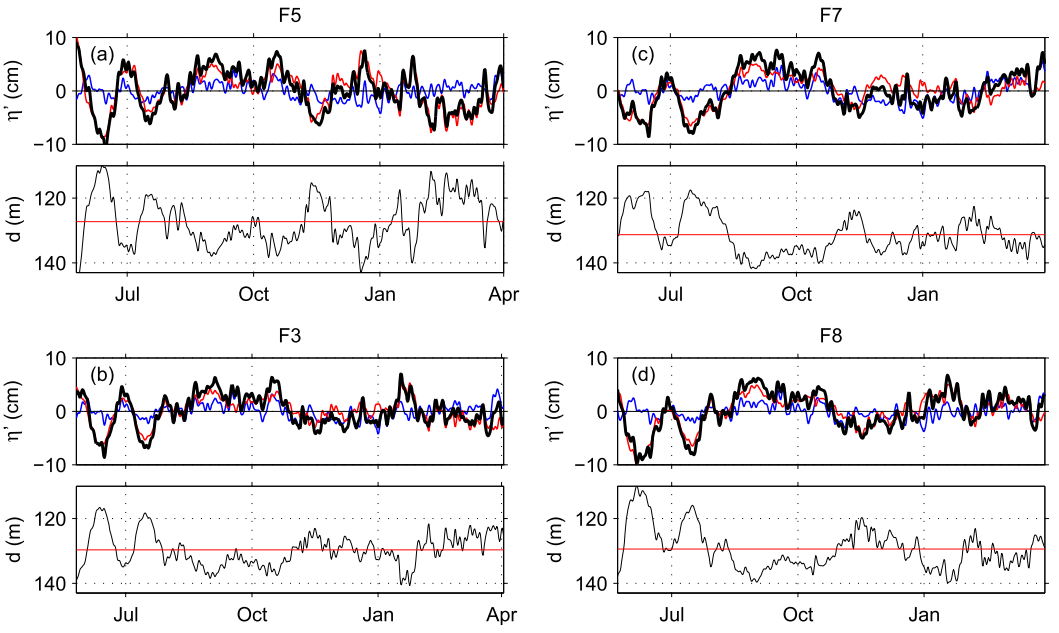

FIG. 11. Sea surface height anomaly η' and pycnocline depth d inferred from the CPIES records at sites (b) F3, (a) F5, (c) F7, and (d) F8 where Spray glider dives are available for calibrations. In the upper panel of each set, the steric contribution η_{ST} inferred from τ_{LP} is red, the mass-loading contribution η_{ML} inferred from p_{LP} is blue. These contributions sum to give the total sea surface anomaly η' at each site (heavy black curve). In the lower panels in each set, the red line shows the record-mean pycnocline depth. Correlations between η' and d in (a)–(d) are 0.92, 0.88, 0.87, and 0.93, respectively.

the η inferred at the four CPIES sites from τ, p, and the GEM lookup tables (Fig. 11) and is as expected since sea surface highs (anticyclones) are accompanied by a depressed pycnocline and thermocline and higher vertically averaged sound speed, while sea surface lows (cyclones) are accompanied by a shoaled thermocline and lower vertically averaged sound speed (e.g., Ramp et al. 2017).

For the calibrated CPIES sites, we can quantify variability in the sea surface height η and the pycnocline depth d. Mesoscale variability in the total sea surface height ($\eta_{TOT} = \eta_{ST} + \eta_{ML}$, which excludes any tidal contributions) arises primarily from variability in the steric component η_{ST}, which is determined from τ_{LP} [in conjunction with the GEM lookup table and Eq. (8)]. The time series of η_{TOT} and η_{ST} anomalies track one another very closely at all sites (see the red and heavy black curves in the upper panels in Fig. 11). While variability in the mass-loading component η_{ML}, which is determined from p_{LP} and Eq. (9), does contribute to the overall sea surface height variability, its variance is less half that of the steric contribution.

At site F5, where the range in η_{TOT} is largest (20-cm range), the range in pycnocline depth is also largest, with d varying between 110- and 150-m depth during the deployment record (Fig. 11a). Errors in pycnocline depth estimated using the PIESs are around 15 m, constituting a significant fraction of the total variability in pycnocline depth at this location. Consistent with expectations (e.g., Gill and Niiler 1973), changes in d mirror and amplify changes in η_{TOT}: for these sites near Palau, an increase in sea surface height of 1 cm is accompanied by a deepening of the pycnocline by about 1.6 m.

The most striking events in the τ'_{LP} and SSH_{sat} records (Fig. 10a) occur early during the deployment period when two anomalies, in mid-June and in mid-July, each manifested as a depressed sea surface and an elevated pycnocline (Fig. 11). At site F5, for example, the sea surface height anomaly η' reached −11 cm and d reached 110-m depth, which is 17 m above the record's time mean. These signals are due to the arrival of two strong cyclonic eddies. The details of their effects on the vertical structure and bottom currents at the CPIES sites and on moored FLEAT instruments deployed closer to the tip of Velasco Reef are reported in Andres et al. (2019).

Hovmöller plots of pycnocline depth anomaly to the east and west of Palau obtained with objectively mapped Spray glider data [see section 2b(2)] corroborate that the mesoscale pycnocline depth typically varies by tens of meters over time scales of weeks (Fig. 12) with arrival of

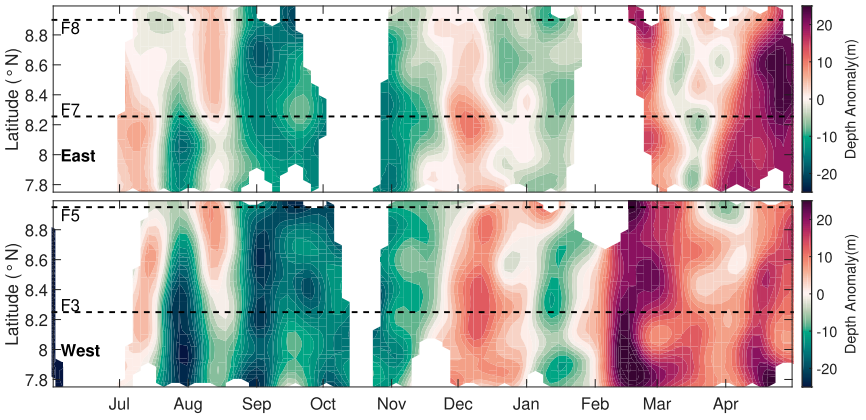

FIG. 12. Objectively mapped anomalies in pycnocline depth (taken as the 1024.5 kg m^{-3} surface) from the Spray glider sections taken along a meridional line (top) east and (bottom) west of the ridge (shaded; times with no data are blank). The latitudes of the nearby CPIESs are indicated with the dashed black lines.

strong mesoscale eddies leading to rapid changes in pycnocline depth. For example, early in the record in the region southwest of the ridge (July–August in the bottom panel of Fig. 12), the pycnocline is depressed at a rate of 3 m day^{-1} to a depth anomaly of −30 m. The latitude-mean depth of the pycnocline is highly correlated across the ridge (r = 0.89), indicating that the zonal length scale of these incident mesoscale features exceeds the 80-km scale of the array. This is consistent with the interpretation that the pycnocline variability on time scales of 20–100 days is due to the westward propagation of mesoscale eddies that by definition have length scales on the order of the first baroclinic Rossby radius, which is about 100 km near Palau (Chelton et al. 1998).

The quality of the correlation between SSH_{sat} and τ_{LP} drops markedly and suddenly across the entire array starting in mid-October and lasting for the duration of each record (Fig. 10a see the green line, Table 4). This drop in correlation is observed both for those instruments that fall directly along a satellite repeat track (F1, F5, F7, and F9) and for those that sites are off-track (F3, F4, F6, and F8) and is accompanied by a marked increase of τ' variance in the band between the local inertial period and the diurnal tide (Figs. 13 and 10b). The aliasing of this high-frequency variability into the satellite record could lead to the degradation of the observed correlation. Also, a known ''hump artifact error'' can lead to poorer than expected correlation between satellite and in situ observations (Jeon et al. 2018).

Based on the tilted phase lines observed on the SSH'_{sat} Hovmöller plot (thin black lines in Fig. 6c), mesoscale eddies in this latitude band are expected to propagate westward across the northern tip of Palau at about 15 km day^{-1} (0.17 m s^{-1}). To investigate in further detail the propagation of these mesoscale eddies through the PIES array and across the Ridge, which sits in a ''hole'' between satellite repeat tracks (Fig. 1b), the lagged correlations of acoustic travel time records are examined using the records from all of the sites (not just the calibrated CPIES records). Since τ'_{LP} (which is 3-day low-pass filtered) contains a component of variability that is unrelated to mesoscale eddies and whose phase propagation direction is southeastward through the array (section 3d), we further filter the acoustic travel time records with a 10-day cutoff period $\tau'_{10\text{-d\_LP}}$ to isolate the mesoscale signals.

Lagged correlations of $\tau'_{10\text{-d\_LP}}$ between sites confirm that the mesoscale signals arrive first at F9 (east of Palau) and then propagate westward across the ridge and finally arrive at F4 about 9 days later (Fig. 14a). F9 is 190 km east of F4 (and 120 km south, but the eddies have a large meridional extent relative to the array and propagate primarily westward). This suggests that the eddies propagate westward across the array at about 21 km day^{-1} (0.24 m s^{-1}), about 25% faster than suggested

TABLE 4. Correlation and regression for τ_{LP} vs SSH_{sat}.

	Whole period	Before 15 Oct 2016	
Site ID	r	r	R (m s cm^{-1})
F1	−0.63	−0.81	−0.97
F3	−0.65	−0.79	−0.55
F4	−0.66	−0.70	−0.47
F5	−0.66	−0.72	−0.54
F6	−0.55	−0.76	−0.50
F7	−0.54	−0.74	−0.52
F8	−0.45	−0.79	−0.52
F9	−0.39	−0.78	−0.62

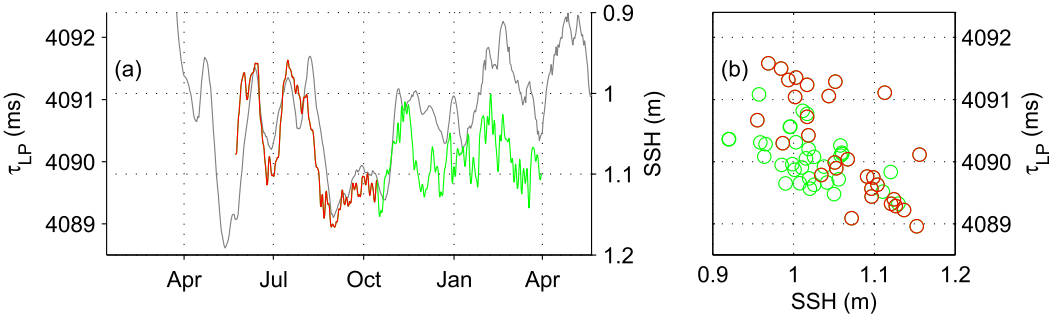

FIG. 13. Example for F7 of the degraded correlation between τ_{LP} and SSH_{sat} from mid-October onward. (a) Time series of τ_{LP} (red and green curve) and SSH_{sat} (gray curve, inverse scale on right). (b) τ_{LP} vs SSH_{sat} before 15 Oct (red circles; $r = -0.76$) and thereafter (green circles, $r = -0.38$). To correspond with the altimeter sampling interval, values in (b) are shown for each time series subsampled to 10-day intervals. The correlation coefficients are both significant (at the 99% and 95% levels, respectively) treating each value subsampled at 10-day intervals as independent.

by the phase lines from altimetry at this latitude (Fig. 6c). Whether this is a real local acceleration warrants further study (perhaps with numerical model output) to test whether there is 1) local acceleration of the eddies as they are advected by the NEC and/or 2) local acceleration of the eddies as they encounter the shallow ridge north of Palau. The sense of phase propagation found by the lagged-correlation analysis is confirmed by CEOF analysis of $\tau'_{10\text{-d\_LP}}$. The CEOF phase structure (Fig. 14b) also shows westward propagation across the array of the first mode (which explains about 76% of the variance).

To test how far in advance one can predict the arrival of a mesoscale eddy on the eastern edge of Palau, we compare $\tau'_{10\text{-d\_LP}}$ at F7 with altimetry to make lagged-correlation maps. At each time step and for each latitude/longitude, the zonally averaged MADT from 130° to 170°E is subtracted from the local total MADT [to remove the effect of large-scale zonal processes and rapid barotropic waves as in section 2b(5) and Fig. 6c]. This filtered MADT is then compared to $\tau'_{10\text{-d\_LP}}$ at F7 at zero lag (Fig. 15a) and at progressively longer leads (Figs. 15b–d). At zero lag there is a large region of strong negative correlation near F7 (as expected, see Figs. 11 and 13a). As the lead (of SSH relative to $\tau'_{10\text{-d\_LP}}$) increases, this patch of negative correlation is progressively farther east. At 60-day lead, the distance between the correlated patch and F7 is 870 km, which suggests that the eddies move westward at about 14.5 km day^{-1} consistent with the slope of the phase lines in Fig. 6c and consistent with the phasing suggested by the CEOF analysis (Fig. 14b). Beyond 60-day lag it is difficult to definitively track this patch of negative correlation farther east as there seem to be regions of spurious correlation in the maps. This may suggest that eddies that reach Palau are generated near 145°E (at least during the 2016/17 FLEAT experiment) or it may simply reflect the noisy eddy field. Regardless, it does seem possible to predict the eddy-related SSH variations near Palau (and the associated subsurface pycnocline displacements) with several month lead time using the filtered MADT. The arrival at Palau of westward-propagating eddies

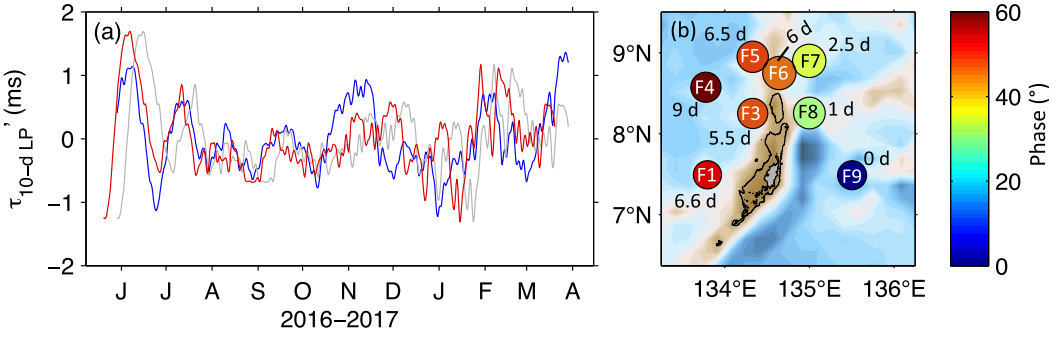

FIG. 14. (a) Time series of $\tau'_{10\text{-d\_LP}}$ at F9 (blue), at F4 (gray), and at F4 lagged by 9 days (red). (b) Spatial functions of mode 1 phase (shading) and amplitude (represented by the area of the circles) for CEOF analysis of $\tau'_{10\text{-d\_LP}}$. For comparison, the annotation indicates the lag (in days) of each site's $\tau'_{10\text{-d\_LP}}$ relative to that at F9.

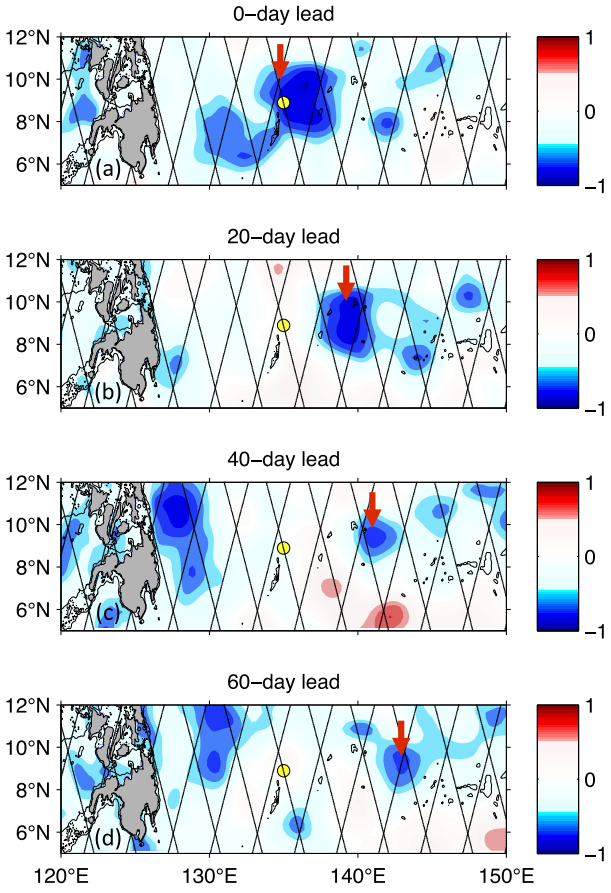

FIG. 15. Maps of correlation between $\tau'_{10\text{-d\_LP}}$ at F7 and filtered MADT at different leads (with the filtered SSH leading $\tau'_{10\text{-d\_LP}}$). Altimetry repeat tracks are indicated (black) as is the location F7 (yellow dot). Red arrow indicates region of negative correlation that propagates from about 143°E toward Palau.

is consistent with the analysis of global satellite altimetry, which shows that these coherent mesoscale features are ubiquitous in the open ocean (Chelton et al. 2011).

d. Superinertial signal

Spectra of τ' [hourly records from which the barotropic and internal tides have been removed according to Eq. (4) and the methods described in section 2a(2)] show that there is a band that contains comparable variance to the mesoscale with the energy falling primarily between 1.1 and 3 days (Fig. 16, pink shading). Energy in this band is present at all sites, though the variance peaks in this band are strongest at sites F1, F3, and F6 and are relatively weak at F9 (this does not define relative amplitudes since these are not calibrated to a common reference pressure, but it is suggestive). Notably, the spectrum for each site has only a very small (or no) peak in the local near-inertial band (from f to 1.2f, where f is the local Coriolis parameter).

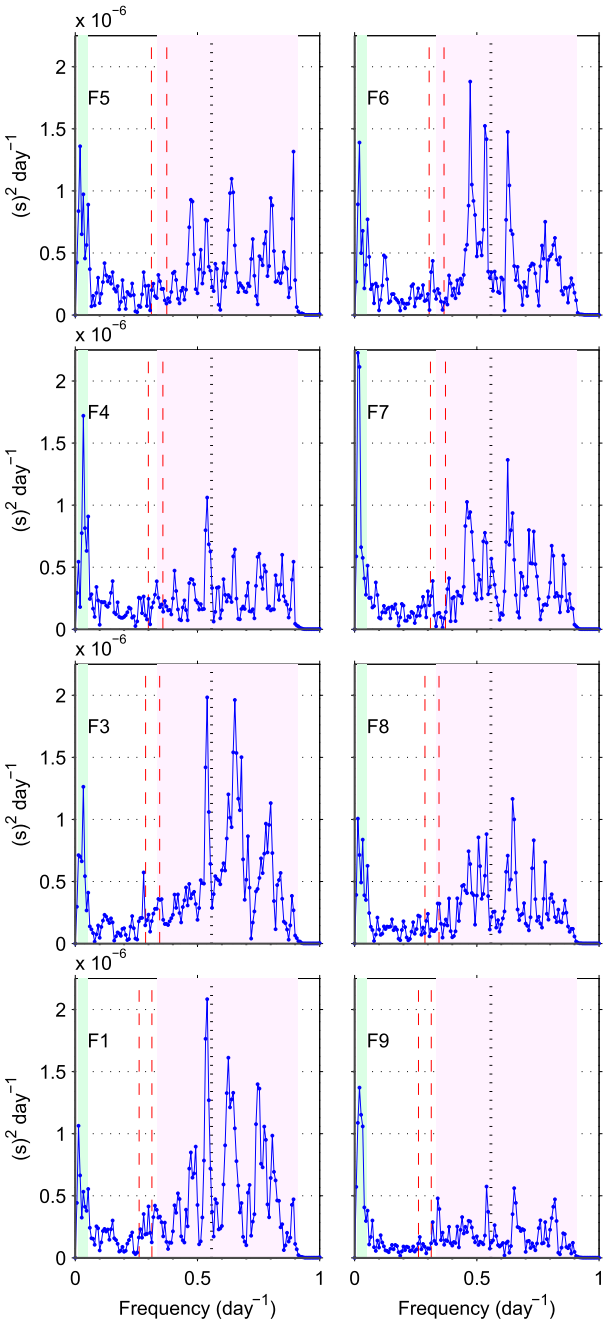

FIG. 16. Spectra of τ' with each site's local near-inertial band (from f to 1.2f, Alford et al. 2016) indicated (red dashed lines). Green shading highlights the mesoscale band (20–100-day period) and pink highlights the superinertial band (1.1–3-day period). For reference, the black dotted lines indicate the inertial peak at a latitude near the Philippines (16.2°N, 43 h).

This lack of a local near-inertial peak is as expected since these waves—if present—are associated with very small isopycnal displacements (and hence little impact on τ). The frequency band of the 1.1–3-day signal indicates that these waves cannot be due to

TABLE 5. Results from CEOF and lagged-correlation analyses of τ'_{BP}.

	First COEF mode		Lagged correlation	
Site ID	Amplitude	Phase (°)	R	Lag (h)
F1	0.35	21.3	0.57	6
F3	0.41	21.6	0.71	5
F4	0.34	7.2	0.75	1
F5	0.38	0.0	1.00	0
F6	0.41	19.8	0.73	4
F7	0.35	15.9	0.66	3
F8	0.35	44.7	0.62	9
F9	0.19	68.9	0.50	16

locally generated near-inertial waves. Here we suggest that the energy in this ''superinertial'' band may be from near-inertial waves that are generated at a higher latitude and propagate southward toward Palau.

To isolate the superinertial signal, the τ' records are bandpass filtered with a long-period cutoff at 10 days to remove the strong mesoscale variability and a short-period cutoff at 1 day. Time series of these bandpassed records τ'_{BP} show a marked increase in amplitude at each site after 15 October 2016 (Fig. 10b) with ''packets'' of high-amplitude signal apparent across multiple sites. Due to the difficulties in interpreting the amplitude of the uncalibrated travel time measurements, we focus instead on the phase relations between the τ'_{BP} time series at each site. Lagged correlations of τ'_{BP} between sites calculated for the records after 15 October 2016 show strong (lagged) correlations between sites: F5 leads all other sites and F9 lags all other sites suggesting southeastward phase propagation of the superinertial signal across the array (Table 5). τ'_{BP} at F9 (which is 129 km east and 162 km south of F5) lags that at F5 by 16 h. The slowest propagation speed between sites is observed between F5 and F6 (separated by 41 km) where the strongest correlation occurs at 4-h lag. This suggests the superinertial signals are propagating as plane waves with roughly 10.2 km h^{-1} (2.8 m s^{-1}) phase speed toward the southeast with a bearing of −32.8° (relative to east).

Results from CEOF analysis of the τ'_{BP} records plotted in Fig. 10b are consistent with the lagged-correlation analysis. The first CEOF mode explains about 60% of the variance in this 1–10-day band (Table 5); the second and third modes explain 13% and 9%, respectively. The phase of this first CEOF mode also suggests southeastward propagation across the array (see the shaded dots in Fig. 17a). As suggested by the time series in Fig. 10b, the amplitude time series of this mode increases in mid-October (Fig. 17b, blue curve) hinting at a seasonal component in the forcing of these waves.

To obtain an estimate of the time-varying amplitude of the superinertial waves, the standard deviation of the CEOF's temporal amplitude function for the first CEOF mode in a moving 120-h (5 day) window is calculated (Fig. 17b, red curve). The correlation between this amplitude time series and the magnitude of the NCEP wind stress is calculated at each latitude/longitude over the North Pacific to generate a correlation map (Fig. 18). This map shows two features of interest. First, there is relatively low correlation between the amplitude of the superinertial waves and the wind stress magnitude at the location of Palau, indicating that these waves are not locally forced. This is consistent with the waves' spectra in which the peak at the local inertial period is small

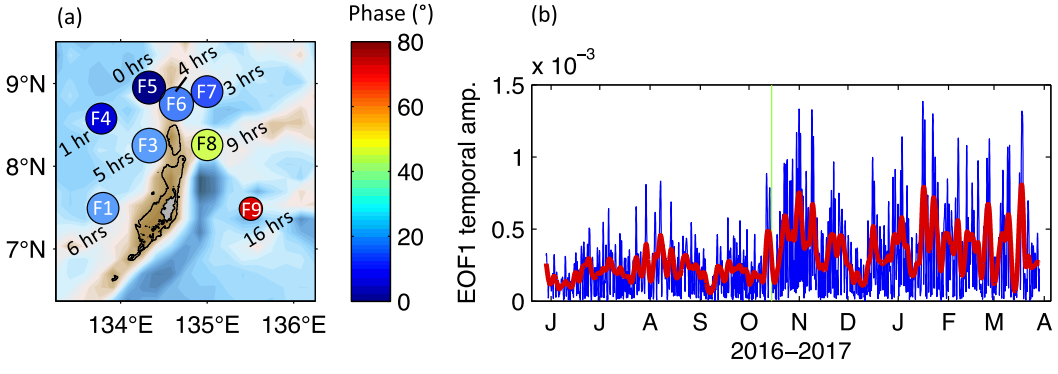

FIG. 17. First empirical mode calculated from CEOF analysis of τ'_{BP}. (a) The spatial functions of first mode CEOF phase (shading) and amplitude (represented by the area of the circles). (b) The corresponding temporal amplitude time series for the first mode (blue curve). For comparison, in (a) the lags (in hours relative to τ'_{HP} at site F5) are annotated; these lags are calculated by finding the maximum correlation between each site and site F5 for τ'_{BP} from mid-October onward [i.e., after the time denoted by the green line in (b)]. In (b) the red curve shows the standard deviation of the temporal amplitude time series in a moving 120-h window (which is used in section 3d as a measure of the time-varying strength of the superinertial waves).

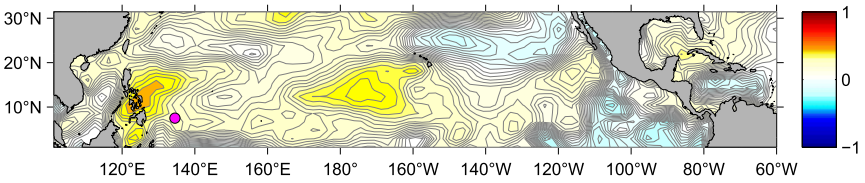

FIG. 18. Correlation map showing 0-lag correlation between wind stress magnitude (calculated from NCEP wind stress) and the strength of the superinertial waves at Palau (i.e., as quantified by the red time series in Fig. 17b). Palau is indicated with the magenta dot.

or absent (Fig. 16). Second, there is a region of strong positive correlation at zero lag between the amplitude of superinertial waves and the wind stress magnitude near the Philippines. The patch of highest correlation ($r > 0.425$) stretches northward to about 16°N where the local inertial period is 43 h (a shorter period than the local inertial period at the PIES array). The horizontal group velocities of internal gravity waves peak at slightly superinertial frequencies, with a reasonable value being around 1.5 m s^{-1}, giving a transit time from the Philippines to Palau (700 km) of around 5 days. For the 5-day moving window used to filter the CEOF amplitude function, this is consistent with our finding of maximum correlation at zero lag.

A preliminary analysis of 3-h interval output from a data-assimilative numerical model, HYCOM (Chassignet et al. 2007), shows a feature constituent with that revealed in Fig. 18. Using the temperature and salinity profiles from HYCOM, we first calculate the time varying round-trip acoustic travel time between 1000 m and the surface (τ_{1000}) in the western Pacific. The model's performance is evaluated by comparing at the PIES sites the calculated τ_{1000} (modeled) with τ_{LP} (observed). The variability captured by the model compares favorably to that measured by the FLEAT PIESs (e.g., that for site F5 is shown in Fig. 19a). Correlation coefficients between τ_{1000} and τ_{LP} at the eight PIES sites show statistically significant values, ranging from 0.35 at F8 to 0.53 at F3.

CEOF analysis applied to the model's τ_{1000} field results in a first mode (which explains 22.1% of total variance at 1–4-day periods) with high amplitude east of the Philippines (Fig. 19b). This coincides with the region where the windstress shows a good correlation with the superinertial waves observed at Palau (Fig. 18). The phase of the first-mode CEOF (Fig. 19c) suggests a southeastward propagation for this mode, which is consistent with the observed propagation of these feature through the array (Fig. 17a). These numerical model results strongly support the hypothesis that the superinertial waves at Palau originate from the region east of Philippines. Further evaluation of the model output and analysis of the superinertial signal within the model framework is the subject of ongoing research.

4. Summary

a. *Variability in the sea surface and pycnocline*

The observations discussed in section 3 demonstrate that SSH near Palau is subject to variability that occurs over a wide range of temporal scales associated with different oceanic processes, some of which are accompanied by substantial displacements of the pycnocline (Fig. 2). How SSH and d are related is strongly process dependent, reflecting the relative contribution of the steric versus the mass-loading contribution to the total SSH associated with each of these processes. For example, sea surface displacements associated with the barotropic tide η_{BT} can reach ±1 m during spring tide around Palau (e.g., Fig. A2a) and have little expression in the pycnocline, since, by definition, η_{BT} contains only a mass-loading signature and no steric component. Signals associated with the internal tide, on the other hand, are mostly subsurface, with pycnocline displacements reaching 5–10 m amplitude for both the diurnal and the semidiurnal bands around Palau (Fig. 8). Sea surface displacements associated with these internal tides are estimated to be between 2 and 5 cm. Variability associated with cyclonic and anticyclonic mesoscale eddies near Palau manifests strongly *both* in the sea surface and in the pycnocline (Fig. 11). For the mesoscale eddies observed during the FLEAT experiment, the SSH:d ratio is about 1:160 (inferred from p, τ, and the GEM lookup table) and the eddies' SSH signals are mostly steric with η_{ST} reaching 10-cm amplitude and η_{ML} reaching only 1-cm amplitude around Palau. As with mesoscale eddies, variability near Palau associated with ENSO events is also strongly expressed both in the sea surface and in the pycnocline (Fig. 5) but the SSH:d ratio is about 1:250 for the 2003–17 period (inferred from tide gauge measurements and Argo profiles), reflecting larger pycnocline displacements for a given SSH displacement than is

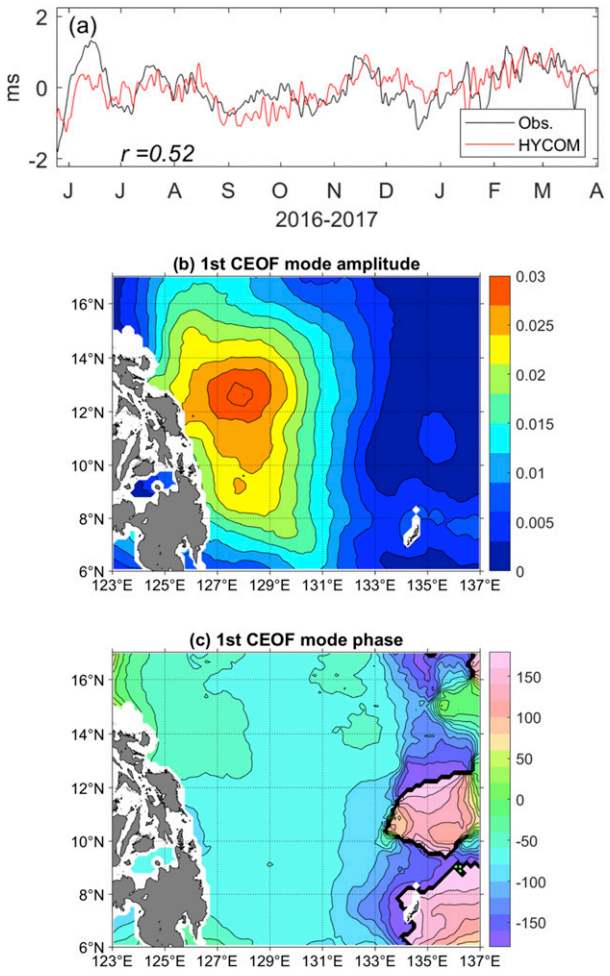

FIG. 19. (a) Time series of observed acoustic echo time anomaly (black) and calculated (red) using output from HYCOM model. The correlation coefficient between them is 0.52. (b) Amplitude and (c) phase of the first-mode CEOF for the calculated acoustic echo time τ_{1000}. The CEOF was applied after filtering the 3-h interval model output at bands between 1 and 4 days.

observed for the eddies. Also, the amplitude of the ENSO signal in SSH is about 20 cm, twice that associated with mesoscale eddies. The differing ratios of SSH:d associated with each of these processes reflect their different steric/mass-loading fractions on SSH.

Table 6 summarizes our results from the PIES observations, showing the contributions to η and d for those processes and sites where these can be inferred from the site's p and τ measurements. These include standard deviations and ranges for η_{BT} [comprising the total sea surface displacement from 8 constituents of the barotropic tide, section 2a(1) and 3a(1)], d_{tide} [the pycnocline displacements for the total semidiurnal plus diurnal internal tide at sites where we have sufficient calibration casts from gliders, and also assuming a mode 1 structure for these internal tides, section 2a(2) and 3a(2)], η_{TOT} [the total sea surface displacement in the mesoscale band comprising the steric η_{ST} and mass-loading contributions η_{ML}, section 2a(4) and 3c], and d_{eddy} (the mesoscale's contribution to pycnocline displacements) where η_{ST} (and hence η_{TOT}) and d_{eddy} are inferred using the lookup tables—but only at the sites where we have the glider calibration casts. We do not know the vertical structure of the variability in the superinertial band (as it may not be well represented by the gravest mode that is captured in the lookup tables), so we do not estimate the superinertial η and d here nor the relative steric/mass-loading contributions to total η in this band. Nevertheless, we note that τ variance in this band is quite tiny compared to that in the other bands (Table 2), so the superinertial η and d signals are likely small as well.

b. *Propagation and predictability*

As discussed in section 3, how signals in these frequency bands move across the FLEAT PIES array is process specific, as is the predictability of the associated SSH variations north of Palau. Notably, as mesoscale eddies move westward through the array across the Kyushu-Palau Ridge, their phase speed is 0.24 m s^{-1}, about 25% faster than observed with altimetry at this latitude east of Palau, suggesting a local acceleration of the eddies, perhaps related to the topography of the ridge. An analytical study suggests that mesoscale eddies can speed up in the presence of closed potential vorticity contours (f/H, where f is the Coriolis parameter and H is the water depth) due to the "Rossby wormhole" effect (Marshall 2011). Despite this slight local speedup, SSH anomalies are quite coherent as they move westward, and lagged correlations suggest it is possible to use altimetry to predict an eddy's SSH (and d) signal near Palau with about 60-day lead.

In contrast to the eddies, signals in the superinertial band have southeastward phase propagation across the FLEAT array, with 2.6 m s^{-1} phase speed. If these are wind forced, the amplitude of packets of these waves arriving at Palau may be tied to seasonal variations in the remote winds and it may be possible to predict when they will be energetic. This remains speculative, however, as we only have a 10-month record in which they manifest starting around October and last through the following April (which is the end of our record). The inferred group speed for these waves (assuming they are generated by the winds near the Philippines) is consistent with that of internal gravity waves (about 1.5 m s^{-1}).

The largest contributors to SSH variations around Palau are the barotropic tide (which is regular and predictable and fairly well represented by tidal models in this region with the M2 tide amplitudes reaching 50 cm) and the SSH variability associated with ENSO events. Though the timing of the SSH increase on Palau

TABLE 6. Summary of results from the PIES observations.

	Tides				Mesoscale eddies					
	Barotropic η_{BT}		Internal d_{tide}		η_{TOT}		d_{eddies}		η_{ML}	
Site ID	Std (cm)	Range (m)	Std (m)	Range (m)	Std (cm)	Range (cm)	Std (m)	Range (m)	Std (cm)	Range (cm)
F1	44	2.18	—	—	—	—	—	—	2	8
F3	43	2.17	4.14	24.0	3	16	5	24	1	8
F4	44	2.18	—	—	—	—	—	—	2	9
F5	43	2.13	6.52	43.7	4	20	7	40	2	9
F6	43	2.11	—	—	—	—	—	—	2	9
F7	42	2.08	2.65	17.8	4	16	6	24	2	11
F8	42	2.06	2.78	16.9	4	17	6	30	1	8
F9	41	2.03	—	—	—	—	—	—	1	8

after an El Niño peaks and relaxes back to a La Niña state is not well constrained (and varies from about 3 to 7 months), the magnitude of this sea level increase is predictable and is well correlated with the Niño-3.4 index's peak value during the El Niño event.

The internal tides (which have only small expression in SSH but a significant expression in d) have a regular component that seems tied to the local spring-neap cycle (and is hence predictable), but this is overlaid with large intermittent variability suggesting local and remote sources that are challenging to predict.

5. Conclusions

Combining in situ measurements from PIESs and Spray gliders with observations from satellite altimetry by Palau has provided a window into the processes that influence sea surface height and pycnocline depth in a low-latitude region where the currents and eddies interact with complex topography. Various aspects of the variability observed here, at both high and low frequencies, still remain to be investigated further. For example, the superinertial signals whose phase propagates southeastward across the array (thus far identified in τ), may have an expression in the sea surface, but its magnitude remains unknown. Though this signal is not well captured by the present altimeters, perhaps this sea surface signal will be resolved by the upcoming Surface Water and Ocean Topography (SWOT) mission (Morrow et al. 2019). In addition, details of the signal propagation from the forcing region to Palau remain to be investigated further, as does the question of whether there are other regions where similar processes lead to superinertial τ (and SSH and d) variability. The internal tide and the extent to which it is phase locked to the barotropic tide is under investigation, as is its observed spatial and temporal variation around Palau. At the lower frequencies, though it seems that SSH variability associated with ENSO events is predictable, it remains to be investigated (perhaps with Argo observations) whether changes in the pycnocline depth are similarly predictable. The deep expression (in bottom pressures and near-bottom currents) of mesoscale eddies, apparent in SSH and τ (pycnocline depth) are examined in more detail elsewhere (Andres et al. 2019).

Finally, comparison of in situ observations of property profiles from Spray glider dives with the concurrent PIESs observations, has demonstrated that a regional approach to travel time calibration (as typically used to study strong western boundary currents like the Gulf Stream or Agulhas) is not applicable near Palau. Due to the abrupt topography, the relation between deep and shallow travel time is highly localized at Palau, and cannot be captured by the coarse spatial resolution of datasets like Argo or WOCE. It remains to be investigated whether this is specific to the region around Palau where the NEC, NECC, and mesoscale eddies impinge on the Kyushu–Palau Ridge, or is true more generally where currents encounter abrupt topography at low latitudes.

Acknowledgments. Support for this research was provided by Office of Naval Research Grants N00014-16-1-2668, N00014-18-1-2406, N00014-15-1-2488, and N00014-15-1-2622. R.C.M. was additionally supported by the Postdoctoral Scholar Program at the Woods Hole Oceanographic Institution, with funding provided by the Weston Howland Jr. Postdoctoral Scholarship. We gratefully acknowledge Chief Scientist H. Wijesekera and the captain and crew of the R/V *Roger Revelle*. We appreciate the invaluable assistance from D.R. Watts, E. Sousa, and M. Kennelly from the University of Rhode Island Graduate School of Oceanography.

APPENDIX

PIES Data Processing and Interpretation with the GEM

This appendix describes the PIES data processing (section a), compares two different calibration processes for the region around Palau to convert τ (as measured at

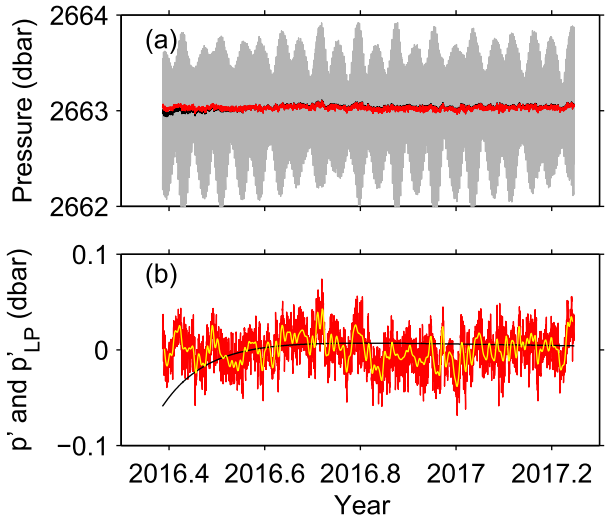

FIG. A1. Example pressure record from site F8. (a) The full pressure record $p_{\mathrm{B\_meas}}$ (gray); the detided record (black); and the dedrifted, detided record (red): $p_{\mathrm{B\_meas}}-p_{\mathrm{drift}}-p_{\mathrm{BT\_tide}} = p + \overline{p}$. (b) The residual, detided hourly bottom pressure p' [red, which is equivalent to the red curve in (a) with $\overline{p}$ subtracted] and the low-pass-filtered record p'_{LP} (yellow); also shown is the removed signal associated with instrument drift, p_{drift} (black).

the instrument depth) to τ_{ref} (section b), and explains the construction of GEM lookup tables (section c).

a. Processing the PIES records

Each PIESs was programmed to measure pressure with a Paroscientific Digiquartz sensor at 10-min intervals giving 6 measures per hour. The standard data processing procedure (Kennelly et al. 2007) combines these to give a single hourly measure of bottom pressure, $p_{\mathrm{B\_meas}}$ (e.g., Fig. A1, gray curve). The two RPIESs (at sites F1 and F4) sampled in rapid mode for part of their deployments for a separate study of solitons. Prior to the standard processing, we subsample the RPIESs' pressure records to mimic the regular sampling schedule. The hourly records are each dedrifted using the method described in Andres et al. (2005) to obtain corrected, hourly bottom pressures p at each of the eight sites, with $p = p_{\mathrm{B\_meas}} - p_{\mathrm{drift}}$ (e.g., Fig. A1, bottom).

Each PIESs was programmed to emit twenty-four 12-kHz pings per hour in bursts of 4 every 10 min and to listen for each ping's first echo from the sea surface. The two RPIESs (at sites F1 and F4) were set up to collect more travel time measurements per hour during their rapid sampling period. As for bottom pressure, we subsample the travel time measurements from the RPIESs to mimic the standard sampling mode of the other instruments before using standard processing methods for each instrument's travel time record. At each site, the 24 individual travel times recorded hourly

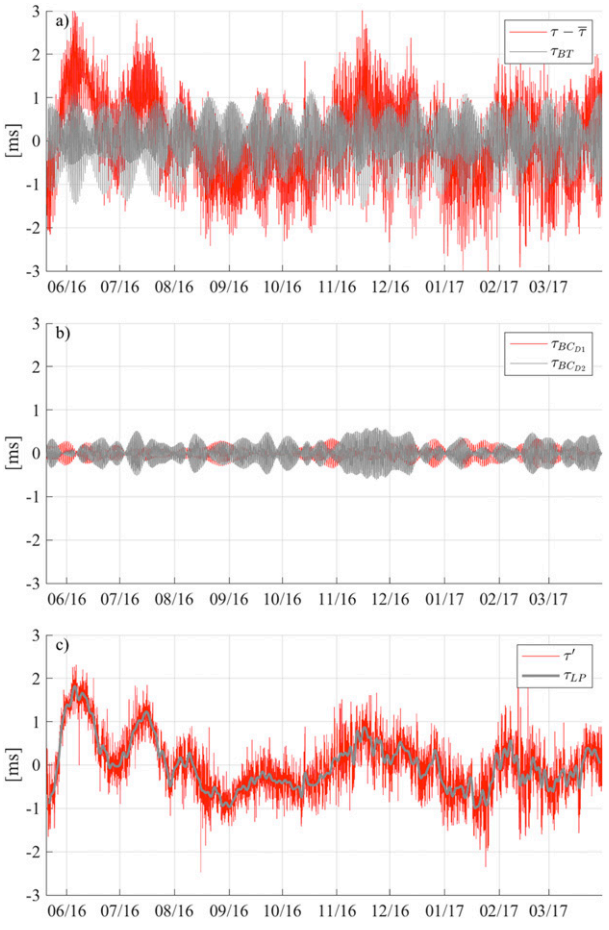

FIG. A2. Example acoustic travel time record from site F8. (a) The full hourly acoustic travel time with only the site's record mean, 3.5150 s, removed ($\tau - \overline{\tau}$, red curve) and the contribution to this hourly record from only the barotropic tide (gray curve). (b) Contribution to τ of the internal diurnal (red curve) and semidiurnal (gray curve) tides. (c) The residual hourly acoustic travel time from which the record mean and barotropic and internal tides have been removed (τ', red curve) and the 3-day low-pass-filtered acoustic travel time (τ'_{LP}, gray curve).

by the instrument are converted to a single, hourly measure, τ (e.g., Fig. A2, top, red curve), using the quartile method (Kennelly et al. 2007).

At each instrument site, we estimate the local $\langle c \rangle$ from the sound speed equation of Del Grosso (1974) and the water property profiles measured by shipboard full-water column hydrographic casts that were taken just after deployment and just prior to recovery (Table 1). Then we calculate the sea surface displacement associated with the barotropic tide, η_{BT}, from each site's pressure record by converting $p_{\mathrm{BT\_tide}}$ to a distance (1 dbar $\approx$ 0.9944 m). Using Eq. (3) with $D = \eta_{\mathrm{BT}}$ and the local $\langle c \rangle$, we calculate τ_{BT}, which is the contribution to τ from the barotropic tide's effect on pathlength (Fig. A2, top, gray curve).

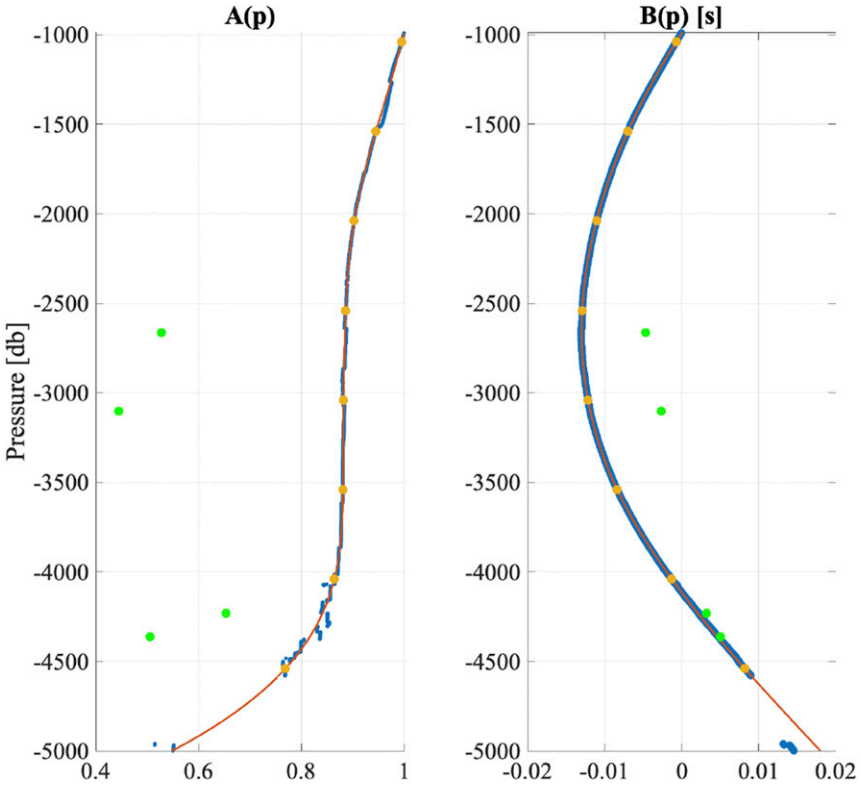

FIG. A3. Regression coefficients $A(p)$ and $B(p)$ determined from both FLEAT and WOCE regional CTD casts (blue dots with a spline fit in red). Green dots indicate coefficients determined at CPIES sites F3, F5, F7, and F8 using instead concurrent Spray glider data.

b. *Calibrating travel times*

To compare vertical acoustic travel times measured at each of the different sites (and depths), measurements are calibrated to a reference pressure, essentially attempting to replace the in situ measurement of vertical travel time with what the measurement would have been were the instrument located at the reference pressure.

For the FLEAT experiment, the repeated presence of concurrent Spray glider measurements over the four CPIES sites during the deployment period allows us first to assess the accuracy of the calibration method that uses historical hydrography in the region, and then to create instead glider-determined calibrations for the CPIESs. Discrepancies between the two calibration methods indicate the presence of horizontal gradients in deep stratification very close to the abrupt topography around Palau, such as those arising from deep geostrophic flows interacting with deep ridges. These discrepancies introduce uncertainties in the applicability of historical regional hydrography for PIES calibration for this region where both deep and upper-ocean (thermocline) variability affect vertical acoustic travel time measurements.

Using 85 WOCE hydrographic CTD casts data spanning 1989–2010 within the latitude range of 4°–11°N and longitude range 131°–138°E, and 26 FLEAT CTD casts at the PIES sites obtained during the observational campaign of 2016–17, we calculate linear regression fits between travel time at a reference pressure and all pressures deeper than this reference (990 dbar was chosen so that the fit parameters obtained here can be compared against those independently obtained from glider data, which only reaches to 1000 dbar). After removing two outlier casts, we are able to determine regression parameters as a function of pressure p down to 5000 dbar with $R^2 > 0.85$, and typically greater than 0.9. The regression parameters $A(p)$ and $B(p)$ enable the referencing of in situ travel time measurements to a common reference depth using the relation

$$\tau'_{990} = A(p)\tau'(p) + B(p), \tag{A1}$$

with

$$\tau' = \tau(p) - \frac{2z(p)}{1500\,\mathrm{m\,s^{-1}}}. \tag{A2}$$

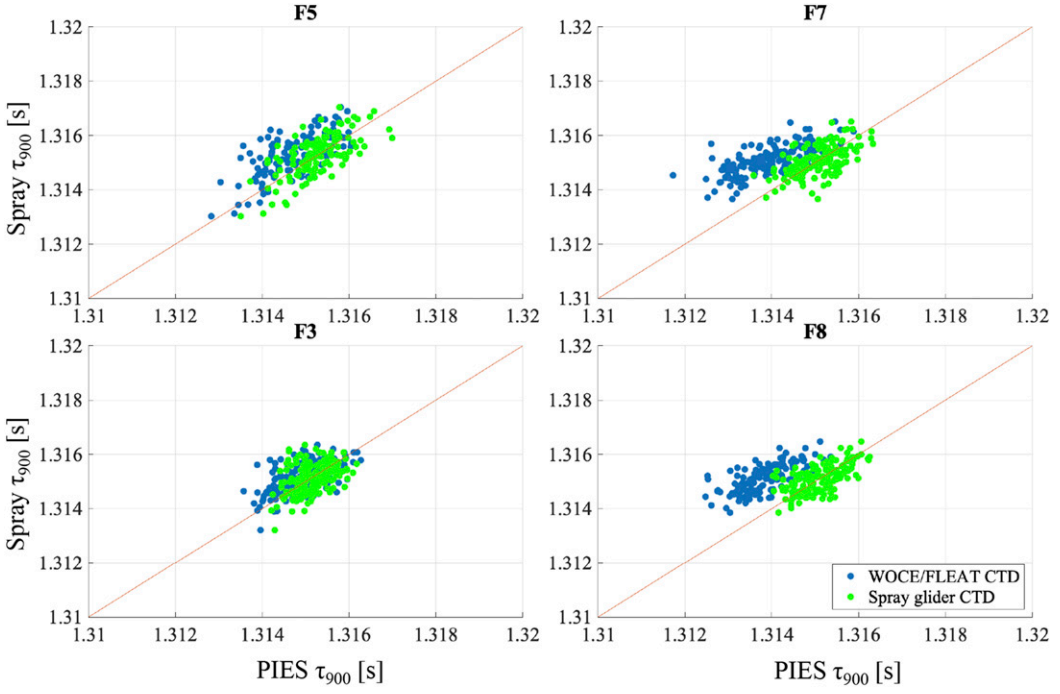

FIG. A4. Comparison of calibrated measured travel times at each site on glider lines. Blue dots are calibrated using WOCE and FLEAT CTD casts, while green dots are calibrated only using concurrent glider profiles. Red line is expected 1–1 relation between glider-estimated and measured τ.

Values for $A(p)$ and $B(p)$, determined using the regional WOCE and FLEAT casts are shown in Fig. A3. As discussed in Meinen and Watts (1998), the closeness of $A(p)$ to 1 indicates that most of the variability in deep travel time in this regional historical dataset is accounted for by variability in travel time *shallower* than the reference depth (with much of this in the thermocline).

Next, the validity of the calibrated PIES travel times [using $A(p)$ and $B(p)$ established with the regional WOCE and FLEAT casts] is determined by comparison to acoustic travel times calculated from concurrent Spray glider profiles at sites F3, F5, F7 and F8, where we consider a concurrent profile to be one that occurs within 0.1° (around 11 km) and within 0.1 of a day. Round-trip travel times between the surface and 990 dbar are computed from glider profiles at these sites and compared with calibrated travel times from the C/PIES (Fig. A4). Since we are comparing acoustic travel time calculated from the temperature and salinity profiles of the gliders (i.e., only the steric component of travel time), we compare them to the hourly CPIES travel times with the barotropic tidal signal removed ($\tau - \tau_{BT}$). In general, the agreement between the calibrated, measured CPIES travel times and those inferred from the gliders is reasonable, with measurements roughly aligned along a 1–1 relation (Fig. A4). However, at sites F7 and F8, to the east of the island, calibrated travel times are biased low by around 1 ms. Furthermore, the ranges of calibrated travel times are larger than the ranges of inferred travel times from concurrent glider measurements. In principle, these discrepancies can arise from a number of sources, including

1) bias in the conductivity–temperature sensors in the Spray gliders on the east of the island;
2) time-mean nonsteric sea level variability that is not captured by travel time estimates calculated from hydrography;
3) regional variability in time-mean atmospheric pressure, leading to errors in assessing the true depth of the CPIES from their pressure sensor; and
4) regional variability in regression parameters $A(p)$ and $B(p)$, implying deep regional variability in the relation between bottom measured τ_{meas} and τ_{990} around the island of Palau.

In comparing the T–S properties of the gliders deployed on either side of the island, we are able to discount 1 as the source of the bias. A bias of 1 ms arising from time-mean nonsteric effects could be generated by sea level variability around 1.5 m, and, assuming a length scale similar to that of Palau (100 km), the inferred depth-uniform geostrophic velocity associated

with such variability would be around 7 m s^{-1}, allowing us to discount item 2 as the source of the bias. A time-mean change of 0.1 atm across the island could account for the bias; however, Palau is a relatively low-lying island with a maximum height of 242 m, so this is unlikely. We are left with item 4 as the most likely source of the discrepancy.

To understand how regional variability in $A(p)$ and $B(p)$ would manifest in Fig. A4, we consider the expression for the full, rather than perturbation travel times:

$$\tau_{990} = A(p)\left[\tau(p) - 2\frac{z(p)}{1500\,\mathrm{m\,s^{-1}}}\right] + B(p) + 2\frac{z(990)}{1500\,\mathrm{m\,s^{-1}}}. \tag{A3}$$

The range of τ_{990} in Fig. A4 is determined by the magnitude of $A(p)$, while the mean values of τ_{990} (setting the bias of the measurements away from the 1–1 line) are determined by the magnitudes of both $A(p)$ and $B(p)$. The observed discrepancies at each site in the mean and range of τ_{990} arise from local variability in $A(p)$ and $B(p)$. Scatter in the relation between glider and PIES travel time arises from the spatial (up to 15 km) and temporal (up to 2 h) offset between the glider profile and PIES measurement, wherein internal waves or other relatively short length scale processes will affect the comparison. Scatter can also arise from temporal variability in sound speed at depths below 990 dbar that are uncorrelated with changes above 990 dbar.

We reevaluate $A(p)$ and $B(p)$ at each of the CPIES sites, this time estimated using concurrent glider data (Fig. A3 green dots, and Fig. A5) and use them to perform a second calibration of the CPIES travel times to 990 dbar (green dots, Fig. A4). As expected, the new calibrations reduce the range of the CPIES measurements to be closer to the range of concurrent glider estimates, and remove the bias in measurements from the 1–1 line. The values for $A(p)$ calculated from the glider are much lower than those calculated from the historical dataset, indicating that at these locations, changes in hydrography below the reference depth (i.e., arising from deep currents) play a significant role in changes in the measured acoustic travel time. Differences in $B(p)$ at sites F7 and F8 are responsible for the bias in the historically calibrated travel times, and they indicate the presence of a time-mean regional difference in the deep hydrography to the east of the island (that is likely not sampled by the historical hydrography since it is fairly confined geographically).

We consider regional variability in these parameters (source 4 in the list above) to be the most likely source of the discrepancy between CPIES travel time and that inferred from concurrent glider measurements. Close to the island, deep geostrophic currents are accelerated around topography, leading to relatively steeply sloped deep isopycnal

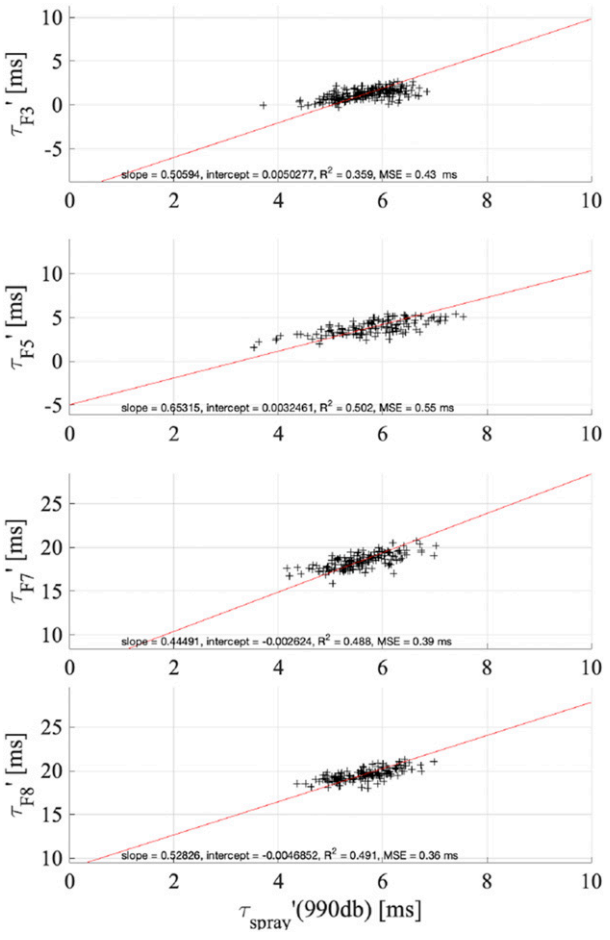

FIG. A5. Regression fits (red line) between travel time calculated from Spray gliders at 990 dbar and CPIES measurements at sites F3, F5, F7, and F8.

gradients. Their time-mean structure would not be captured in regionally averaged historical hydrography, and their variability leads to deep variability in the measured τ that is not captured by variations in thermocline depth.

In summary, it seems that the applicability of a calibration based on regional hydrographic data is inaccurate for calibrating at least some of the instruments due to interactions between deep currents and topography. Unlike regions such as the Gulf Stream, the relation between deep and shallow travel time is highly localized at Palau, and a regional approach to travel time calibration fails. As such, we calibrate only the CPIES located at sites F3, F5, F7, and F8 using the concurrent Spray glider data to construct regression parameters for each of the sites.

c. *Construction of the GEM*

The calibrated travel times τ_{990} can be empirically related to hydrographic profiles of temperature and salinity using the method of the GEM. In constructing

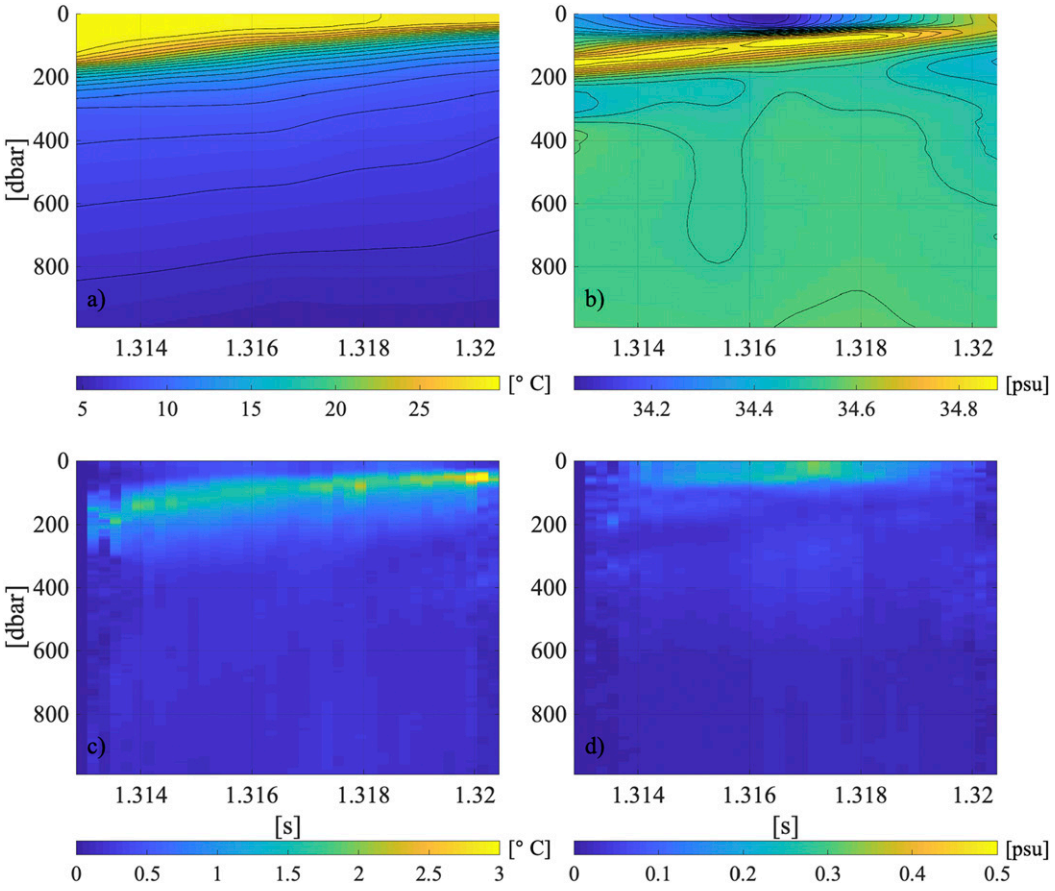

FIG. A6. (a),(b) GEM fields for temperature and salinity. (c),(d) RMS error estimates for temperature and salinity from GEM.

the GEM lookup table we follow the method described in Meinen and Watts (2000), and here we simply outline the method and the data sources that we used in our application near Palau.

Given the availability of more than 7000 Spray glider profiles down to almost 1000-m depth in the region close to Palau during the observational period, we form our hydrographic database using only these data along with 26 CTD casts taken at the PIES sites during deployment and recovery cruises. By calculating the round-trip vertical acoustic travel times associated with each of the profiles, the GEM essentially allows us to construct a lookup table of vertical profiles for T and S for each C/PIES travel time measurement. In contrast to the calibration of travel time described in the previous section, we use all suitable glider profiles to construct a single GEM for all C/PIES sites (only local subsets of the data were used to construct the calibration of travel time at each individual site). The assumption here is that deep variability in travel time is strongly affected by local bathymetry and varies over small horizontal spatial scales (that are set by bathymetric features), while shallow variability in travel time is associated with regional variations in the large and mesoscale currents and has larger horizontal correlation scales.

The hydrographic data are gridded to 1-dbar vertical resolution, and the upper 11 dbar are set to have the same temperature and salinities as at 12 dbar to fill in the gaps and ensure a consistent treatment of the upper mixed layer. Profiles that do not reach 990 dbar are discarded. Vertical acoustic travel times and geopotential anomaly computed from each of the profiles exhibit a dominantly linear correlation, justifying the GEM approach in this region: profiles associated with longer (shorter) vertical travel times are consistently associated with shallower (deeper) thermoclines. A salinity maximum is present at the thermocline, with the freshest waters at the surface (Fig. A6). As expected in this tropical region of the ocean, seasonal cycles are small compared to other modes of variability and we did not attempt to deseason the measured travel times (Watts et al. 2001).

The GEM lookup is formed using spline fits at 1-dbar pressure intervals to the τ-ordered hydrographic profiles.

Errors are estimated from the standard deviations of temperature and salinity in each pressure and travel time bin (0.2 ms), exhibiting around 2°C uncertainty in temperature at the thermocline corresponding to a vertical thermocline displacement of 10–20 m (Fig. A6).

Thermocline displacement can be computed directly from the GEM lookup, but in order to quantify errors in displacement, a second lookup table using the same glider data is constructed relating τ_{990} and thermocline depth (see Tracey et al. 1997). The total error in thermocline depth associated with each travel time measurement is then associated with the two steps in the process: converting τ_{meas} to τ_{990}, and converting τ_{990} to thermocline depth. Errors in the first step contain two components, a measurement error assumed to be 0.12 ms (which is the root-mean-square of the scatter in the hourly data divided by the square root of the degrees of freedom in the 72-h low-pass-filtered records)—see Meinen and Watts (1998), and the mean-square error in the regression between τ_{meas} and τ_{990} (Fig. A5—around 0.4 ms). Errors in the second step arise from the mean-square error around the regression fit between τ_{990} and a specified thermocline depth (which corresponds to the 1024.5 kg m^{-3} isopycnal surface); these are found to be approximately 10 m. The total error in thermocline depth associated with each τ_{meas} is then computed using a Monte Carlo technique, creating ensembles of normally distributed τ_{990} associated with each τ_{meas}, and then ensembles of normally distributed thermocline depth associated with each τ_{990}. In doing this, we estimate that errors in thermocline depth at each site range from 13 to 15 m, a significant fraction of the total observed depth range of around 40 m at Palau.

REFERENCES

Alford, M. H., J. A. MacKinnon, H. L. Simmons, and J. D. Nash, 2016: Near-inertial internal gravity waves in the ocean. *Annu. Rev. Mar. Sci.*, **8**, 95–123, https://doi.org/10.1146/annurev-marine-010814-015746.

Andres, M., M. Wimbush, J.-H. Park, K. L. Tracey, D. R. Watts, W. Teague, D. A. Mitchell, and H. Ichikawa, 2005: East China Sea Kuroshio 2002-2004 data report. University of Rhode Island GSO Tech. Rep. 2005-02, 48 pp., https://digitalcommons.uri.edu/cgi/viewcontent.cgi?article=1011&context=physical_oceanography_techrpts.

——, J. Yang, and Y.-O. Kwon, 2012: Adjustment of a wind-driven two-layer system with mid-basin topography. *J. Mar. Res.*, **70**, 851–882, https://doi.org/10.1357/002224012806770946.

——, and Coauthors, 2019: Eddies, topography, and the abyssal flow by the Kyushu-Palau Ridge near Velasco Reef. *Oceanography*, **32**, 46–55, https://doi.org/10.5670/oceanog.2019.410.

Arbic, B. K., J. G. Richman, J. F. Shriver, P. G. Timko, E. J. Metzger, and A. J. Wallcraft, 2012: Global modeling of internal tides within an eddying ocean general circulation model. *Oceanography*, **25**, 20–29, https://doi.org/10.5670/oceanog.2012.38.

Baker-Yeboah, S., D. R. Watts, and D. Byrne, 2009: Measurements of sea surface height variability in the eastern South Atlantic from pressure-sensor equipped inverted echo sounders: Baroclinic and barotropic components. *J. Atmos. Oceanic Technol.*, **26**, 2593–2609, https://doi.org/10.1175/2009JTECHO659.1.

Chassignet, E. P., H. E. Hurlburt, O. M. Smedstad, G. R. Halliwell, P. J. Hogan, A. J. Wallcraft, R. Baraille, and R. Bleck, 2007: The HYCOM (Hybrid Coordinate Ocean Model) data assimilative system. *J. Mar. Syst.*, **65**, 60–83, https://doi.org/10.1016/j.jmarsys.2005.09.016.

Chelton, D. B., R. A. DeSzoeke, M. G. Schlax, K. El Naggar, and N. Siwertz, 1998: Geographical variability of the first baroclinic Rossby radius of deformation. *J. Phys. Oceanogr.*, **28**, 433–460, https://doi.org/10.1175/1520-0485(1998)028<0433:GVOTFB>2.0.CO;2.

——, M. G. Schlax, and R. Samelson, 2011: Global observations of nonlinear mesoscale eddies. *Prog. Oceanogr.*, **91**, 167–216, https://doi.org/10.1016/j.pocean.2011.01.002.

Church, J. A., and N. J. White, 2011: Sea-level rise from the late 19th to the early 21st century. *Surv. Geophys.*, **32**, 585–602, https://doi.org/10.1007/s10712-011-9119-1.

CMEMS, 2017: Delayed and Near-Real-Time Global All-Sat L4 Altimetry. Accessed 7 July 2017, http://marine.copernicus.eu.

Del Grosso, V. A., 1974: New equation for the speed of sound in natural waters (with comparisons to other equations). *J. Acoust. Soc. Amer.*, **56**, 1084–1091, https://doi.org/10.1121/1.1903388.

Donohue, K. A., D. R. Watts, K. L. Tracey, A. D. Greene, and M. Kennelly, 2010: Mapping circulation in the Kuroshio extension with an array of current and pressure recording inverted echo sounders. *J. Atmos. Oceanic Technol.*, **27**, 507–527, https://doi.org/10.1175/2009JTECHO686.1.

Egbert, G. D., and S. Y. Erofeeva, 2002: Efficient inverse modeling of barotropic ocean tides. *J. Atmos. Oceanic Technol.*, **19**, 183–204, https://doi.org/10.1175/1520-0426(2002)019<0183:EIMOBO>2.0.CO;2.

Gill, A., and P. Niiler, 1973: The theory of the seasonal variability in the ocean. *Deep-Sea Res. Oceanogr. Abstr.*, **20**, 141–177, https://doi.org/10.1016/0011-7471(73)90049-1.

Holgate, S. J., and Coauthors, 2013: New data systems and products at the permanent service for mean sea level. *J. Coastal Res.*, **29**, 493–504, https://doi.org/10.2112/jcoastres-d-12-00175.1.

Horel, J., 1984: Complex principal component analysis: Theory and examples. *J. Climate Appl. Meteor.*, **23**, 1660–1673, https://doi.org/10.1175/1520-0450(1984)023<1660:CPCATA>2.0.CO;2.

Jeon, C., J.-H. Park, D. G. Kim, E. Kim, and D. Jeon, 2018: Comparison of measurements from pressure-recording inverted echo sounders and satellite altimetry in the North Equatorial Current region of the western Pacific. *Ocean Sci. J.*, **53**, 207–213, https://doi.org/10.1007/s12601-018-0012-4.

Johnston, T. M. S., and Coauthors, 2019: FLEAT: A multiscale observational and modeling program to understand how topography affects flows in the western North Pacific. *Oceanography*, **32**, 10–21, https://doi.org/10.5670/oceanog.2019.407.

Kalnay, E., and Coauthors, 1996: The NCEP/NCAR 40-Year Reanalysis Project. *Bull. Amer. Meteor. Soc.*, **77**, 437–472, https://doi.org/10.1175/1520-0477(1996)077<0437:TNYRP>2.0.CO;2.

Kennelly, M. A., K. L. Tracey, and D. R. Watts, 2007: Inverted echo sounder data processing manual. University of Rhode Island GSO Tech. Rep. 2007-02, 89 pp., https://digitalcommons.uri.edu/cgi/viewcontent.cgi?article=1001&context=physical_oceanography_techrpts.

L'Heureux, M. L., D. C. Collins, and Z.-Z. Hu, 2013: Linear trends in sea surface temperature of the tropical Pacific Ocean and implications for the El Niño–Southern Oscillation. *Climate Dyn.*, **40**, 1223–1236, https://doi.org/10.1007/s00382-012-1331-2.

Li, Q., D. M. Farmer, T. F. Duda, and S. Ramp, 2009: Acoustical measurement of nonlinear internal waves using the inverted echo sounder. *J. Atmos. Oceanic Technol.*, **26**, 2228–2242, https://doi.org/10.1175/2009JTECHO652.1.

Marshall, D. P., 2011: Rossby wormholes. *J. Mar. Res.*, **69**, 309–330, https://doi.org/10.1357/002224011798765213.

Meinen, C. S., 2001: Structure of the North Atlantic current in stream-coordinates and the circulation in the Newfoundland basin. *Deep-Sea Res. I*, **48**, 1553–1580, https://doi.org/10.1016/S0967-0637(00)00103-5.

——, and D. R. Watts, 1998: Calibrating inverted echo sounders equipped with pressure sensors. *J. Atmos. Oceanic Technol.*, **15**, 1339–1345, https://doi.org/10.1175/1520-0426(1998)015<1339:CIESEW>2.0.CO;2.

——, and ——, 2000: Vertical structure and transport on a transect across the North Atlantic Current near 42°N: Time series and mean. *J. Geophys. Res.*, **105**, 21 869–21 892, https://doi.org/10.1029/2000JC900097.

Morrow, R., and Coauthors, 2019: Global observations of fine-scale ocean surface topography with the Surface Water and Ocean Topography (SWOT) Mission. *Front. Mar. Sci.*, **6**, 232, https://doi.org/10.3389/fmars.2019.00232.

Munk, W. H., and D. E. Cartwright, 1966: Tidal spectroscopy and prediction. *Philos. Trans. Roy. Soc. London*, **259A**, 533–581, https://doi.org/10.1098/rsta.1966.0024.

Nash, J. D., S. M. Kelly, E. L. Shroyer, J. N. Moum, and T. F. Duda, 2012: The unpredictable nature of internal tides on continental shelves. *J. Phys. Oceanogr.*, **42**, 1981–2000, https://doi.org/10.1175/JPO-D-12-028.1.

NCEP, 2018: NCEP/NCAR Reanalysis 2: Windstress. NOAA Physical Sciences Laboratory, accessed 9 April 2018, https://www.esrl.noaa.gov/psd/data/gridded/data.ncep.reanalysis.pressure.html.

NCEP/NOAA, 2018: Monthly Niño-3.4 Index. NOAA Physical Sciences Laboratory, accessed 11 July 2018, https://www.esrl.noaa.gov/psd/data/correlation/nina34.data.

Park, J.-H., and D. R. Watts, 2006: Internal tides in the southwestern Japan/East Sea. *J. Phys. Oceanogr.*, **36**, 22–34, https://doi.org/10.1175/JPO2846.1.

PSMSL, 2019: RLR monthly sea level. Permanent Service for Mean Sea Level, accessed 4 April 2019, https://www.psmsl.org.

Qiu, B., and S. Chen, 2005: Variability of the Kuroshio Extension jet, recirculation gyre, and mesoscale eddies on decadal time scales. *J. Phys. Oceanogr.*, **35**, 2090–2103, https://doi.org/10.1175/JPO2807.1.

Rainville, L., and R. Pinkel, 2006: Propagation of low-mode internal waves through the ocean. *J. Phys. Oceanogr.*, **36**, 1220–1236, https://doi.org/10.1175/JPO2889.1.

Ramp, S., J. A. Colosi, P. F. Worcester, F. L. Bahr, K. D. Heaney, J. A. Mercer, and L. J. Uffelen, 2017: Eddy properties in the subtropical countercurrent, western Philippine Sea. *Deep-Sea Res. I*, **125**, 11–25, https://doi.org/10.1016/j.dsr.2017.03.010.

Ray, R. D., and G. T. Mitchum, 1997: Surface manifestation of internal tides in the deep ocean: Observations from altimetry and island gauges. *Prog. Oceanogr.*, **40**, 135–162, https://doi.org/10.1016/S0079-6611(97)00025-6.

Savage, A. C., and Coauthors, 2017: Frequency content of sea surface height variability from internal gravity waves to mesoscale eddies. *J. Geophys. Res. Oceans*, **122**, 2519–2538, https://doi.org/10.1002/2016JC012331.

Schönau, M. C., and D. L. Rudnick, 2015: Glider observations of the north equatorial current in the western tropical Pacific. *J. Geophys. Res. Oceans*, **120**, 3586–3605, https://doi.org/10.1002/2014JC010595.

——, and Coauthors, 2019: The end of an El Niño: A view from Palau. *Oceanography*, **32**, 32–45, https://doi.org/10.5670/oceanog.2019.409.

Tracey, K. L., S. D. Howden, and D. R. Watts, 1997: IES calibration and mapping procedures. *J. Atmos. Oceanic Technol.*, **14**, 1483–1493, https://doi.org/10.1175/1520-0426(1997)014<1483:ICAMP>2.0.CO;2.

Wang, B., X. Luo, Y.-M. Yang, W. Sun, M. A. Cane, W. Cai, S.-W. Yeh, and J. Liu, 2019: Historical change of El Niño properties sheds light on future changes of extreme El Niño. *Proc. Natl. Acad. Sci. USA*, **116**, 22 512–22 517, https://doi.org/10.1073/pnas.1911130116.

Watts, D. R., C. Sun, and S. Rintoul, 2001: A two-dimensional gravest empirical mode determined from hydrographic observations in the Subantarctic Front. *J. Phys. Oceanogr.*, **31**, 2186–2209, https://doi.org/10.1175/1520-0485(2001)031<2186:ATDGEM>2.0.CO;2.

Wolanski, E., O. Colin, J. Naithani, E. Deleersnijder, and Y. Golbuu, 2004: Large amplitude, leaky, island-generated, internal waves around Palau, Micronesia. *Estuarine Coastal Shelf Sci.*, **60**, 705–716, https://doi.org/10.1016/j.ecss.2004.03.009.

Zeiden, K. L., D. L. Rudnick, and J. A. MacKinnon, 2019: Glider observations of a mesoscale oceanic island wake. *J. Phys. Oceanogr.*, **49**, 2217–2235, https://doi.org/10.1175/JPO-D-18-0233.1.